INSTITUT FÜR KERNPHYSIK, UNIVERSITÄT FRANKFURT

60486 Frankfurt, August–Euler–Strasse 6, Germany

Charged Particle Production in Proton-, Deuteron-, Oxygen- and Sulphur-Nucleus Collisions at 200 GeV per Nucleon

Abstract

The transverse momentum and rapidity distributions of net protons and negatively charged hadrons have been measured for minimum bias proton–nucleus and deuteron–gold interactions, as well as central oxygen–gold and sulphur–nucleus collisions at 200 GeV per nucleon. The rapidity density of net protons at midrapidity in central nucleus–nucleus collisions increases both with target mass for sulphur projectiles and with the projectile mass for a gold target. The shape of the rapidity distributions of net protons forward of midrapidity for d+Au and central S+Au collisions is similar. The average rapidity loss is larger than 2 units of rapidity for reactions with the gold target. The transverse momentum spectra of net protons for all reactions can be described by a thermal distribution with 'temperatures' between 145 ± 11 MeV (p+S interactions) and 244 ± 43 MeV (central S+Au collisions). The multiplicity of negatively charged hadrons increases with the mass of the colliding system. The shape of the transverse momentum spectra of negatively charged hadrons changes from minimum bias p+p and p+S interactions to p+Au and central nucleus-nucleus collisions. The mean transverse momentum is almost constant in the vicinity of midrapidity and shows little variation with the target and projectile masses. The average number of produced negatively charged hadrons per participant baryon increases slightly from p+p, p+A to central S+S,Ag collisions.

arXiv:hep-ex/9711001v1 1 Nov 1997

The NA35 Collaboration:

T. Alber[10], H. Appelshäuser[6], J. Bächler[5,a], J. Bartke[4], H. Białkowska[12], M.A. Bloomer[3], R. Bock[5], W.J. Braithwaite[10], D. Brinkmann[6], R. Brockmann[5], P. Bunčić[5,b], P. Chan[10], J.G. Cramer[10], P.B. Cramer[10], I. Derado[9], V. Eckardt[9], J. Eschke[6,c], C. Favuzzi[2], D. Ferenc[13], B. Fleischmann[5], P. Foka[5,b], P. Freund[9], M. Fuchs[6], M. Gaździcki[6], E. Gładysz[4], J. Grebieszkow[11], J. Günther[6], J.W. Harris[3,d], M. Hoffmann[7], P. Jacobs[3], S. Kabana[6,e], K. Kadija[9,13], R. Keidel[8], M. Kowalski[4], A. Kühmichel[6], J.Y. Lee[6], A. Ljubičić jr.[13,f], S. Margetis[3,g], J.T. Mitchell[3,f], R. Morse[3], E. Nappi[2], G. Odyniec[3], G. Paić[5,13], A.D. Panagiotou[1], A. Petridis[1], A. Piper[8], F. Posa[2], A.M. Poskanzer[3], F. Pühlhofer[8], W. Rauch[9], R. Renfordt[6], W. Retyk[11], D. Röhrich[6], G. Roland[6], H. Rothard[6], K. Runge[7], A. Sandoval[5], N. Schmitz[9], E. Schmoetten[7], R. Sendelbach[6], P. Seyboth[9], J. Seyerlein[9], E. Skrzypczak[11], P. Spinelli[2], R. Stock[6], H. Ströbele[6], L. Teitelbaum[3], S. Tonse[3], T.A. Trainor[10], G. Vasileiadis[1], M. Vassiliou[1], G. Vesztergombi[9], D. Vranic[13], S. Wenig[6], B. Wosiek[9,4], X. Zhu[10]

[1]Department of Physics, University of Athens, Athens, Greece, [2]Dipartimento di Fisica, Università di Bari and INFN Bari, Bari, Italy, [3]Lawrence Berkeley Laboratory, Berkeley, CA, USA, [4]Institute of Nuclear Physics, Cracow, Poland, [5]Gesellschaft für Schwerionenforschung (GSI), Darmstadt, Fed. Rep. of Germany, [6]Fachbereich Physik der Universität, Frankfurt, Fed. Rep. of Germany (IKF), [7]Fakultät für Physik der Universität, Freiburg, Fed. Rep. of Germany, [8]Fachbereich Physik der Universität, Marburg, Fed. Rep. of Germany, [9]Max–Planck–Institut für Physik, München, Fed. Rep. of Germany, [10]University of Washington, Seattle, USA, [11]Institute for Experimental Physics, University of Warsaw, Warsaw, Poland, [12]Institute for Nuclear Studies, Warsaw, Poland, [13]Rudjer Bošković Institute, Zagreb.
[a]Now at CERN
[b]Now at IKF
[c]Now at GSI
[d]Now at Yale University, New Haven, CT, USA
[e]Now at University of Bern, Bern, Switzerland
[f]Now at Brookhaven National Laboratory, Upton, NY, USA
[g]Now at Kent State University, Kent, OH, USA

1. Introduction

In order to investigate and understand the dynamics of relativistic nucleus-nucleus collisions, it is important to have information on the rapidity and transverse momentum distributions of nucleons participating in the interaction and of particles produced in the collisions, all as a function of the size of the system and of the impact parameter. The differences of particle distributions from proton–proton, proton–nucleus and finally nucleus–nucleus interactions may provide the key to understanding any non-hadronic effects that may appear in central nucleus–nucleus collisions. Ultimately these distributions might be used to determine the behavior of strongly interacting matter at high densities and temperatures.

New results from the measurement of collisions of very heavy nuclei at the BNL AGS and CERN SPS [1, 2] can best be understood by comparison to simpler systems of lighter projectiles and targets. We report results from the NA35 experiment at the CERN SPS on the rapidity and transverse momentum distributions of negatively charged hadrons h^- and participant protons, measured in proton–nucleus, deuteron–gold, oxygen–gold and sulphur–nucleus collisions at 200 GeV per nucleon. A small subset of the present data (S+S collisions) has already been published [3] and has been compared to various theoretical predictions ([4, 5, 6]). The transverse momentum and rapidity distributions provide information on the degree of stopping, thermalization, expansion and flow effects in the collisions. Furthermore, the participant proton rapidity distributions may be used to determine the baryon density or the baryo-chemical potential as a function of rapidity, which constrains model calculations of the dynamics of particle production. The present study is complementary to transverse and forward energy measurements already reported from NA35 [7] which provided global information on the collision dynamics. It is also supplementary to previous strange particle production measurements [8, 9, 10, 11] which are the basis for the determination of the chemical freeze-out conditions. All of this information helps to obtain a consistent picture of the entire reaction process. In particular, it will facilitate detailed comparisons with model calculations (e.g. [4, 12, 13, 14, 15]).

2. Experiment NA35

Experiment NA35 at the CERN SPS studies collisions of p, d, ^{16}O and ^{32}S projectiles of 200 GeV per nucleon incident energy ($\sqrt{s_{NN}}$=19.4 GeV) with nuclear targets. The main detectors are two large-volume tracking devices: a streamer chamber (SC) inside a 1.5 Tesla vertex magnet (VTM) and a time projection chamber (TPC) positioned downstream of the magnet. Both detectors record the space trajectories of charged particles from which the particle momenta are derived. The acceptances of the detectors for negatively charged hadrons are complementary to each other and cover the full phase space with some overlap. Central events are usually selected by the absence of projectile spectators in the veto calorimeter placed in the beam line downstream of all detectors (see e.g. [3, 7, 11, 16]).

The objective of the experiment is to measure the hadronic final state in nucleus–nucleus collisions. In addition to negatively and positively charged particles, weak decays of charged and neutral particles can be detected in the streamer chamber. The analysis of the streamer chamber pictures has been fully automated [16], which not only resulted in an increase of the measuring rate by an order of magnitude but also allowed for a complete simulation of the detector based on the GEANT-package. The results discussed in the following are mainly based on the automated analysis but traditional measurements have been included where appropriate. The TPC identifies charged particles by multiple sampling of the specific ionisation with a dE/dx resolution of about 5-6%. It covers the momentum range of the relativistic rise of the energy loss. This makes particle identification using statistical methods possible. Combining both detectors, spectra of negatively charged hadrons h^-, K_S^0, K^+, K^-, net protons ($p - \overline{p}$), Λ, $\overline{\Lambda}$ and $\overline{p}$ are obtained. Thus information on practically all baryons and mesons in the final hadronic state can be accessed with large phase space coverage. This paper will focus on rapidity and transverse momentum spectra of net (mainly participating) protons and negatively charged hadrons (primarily pions).

In order to accomplish large phase space coverage in collisions with very different particle multiplicities (from p+S to S+Au) and track densities in the laboratory, data were taken in three different experimental setups. Proton- and the oxygen-induced reactions were studied using the (standard) streamer chamber configuration (SETUP I) described in [8, 16, 17]. The nuclear target was placed 11 cm upstream of the 2.0 × 1.2 × 0.72 m^3 streamer chamber (external target) which is the main tracking device inside the 1.5 T magnetic field of the superconducting vertex magnet. In addition p+S interactions were recorded with a target placed inside the streamer chamber (internal target). Charged particles created tracks of streamers of about 1 mm diameter and 1 cm length along their path through the sensitive volume. Three cameras, each equipped with a two-stage magnetically focusing image intensifier of about 2500-fold gain, recorded the events with a demagnification of 30 on 70 mm film. For the ^{32}S induced reactions the track density in the central region along the beam direction ($\Theta_{lab} \leq 5°$) is so high that individual tracks cannot be separated due to the projective readout of the streamer chamber by stereoscopic cameras. Therefore, the streamer chamber geometry was modified by the

insertion of an opaque foil of a trapezoidal shape close to the beam axis reducing the projected track density in that region. In addition, another opaque foil screened the lower half of the streamer chamber in order to further reduce the track density. This modified configuration is called SETUP II.
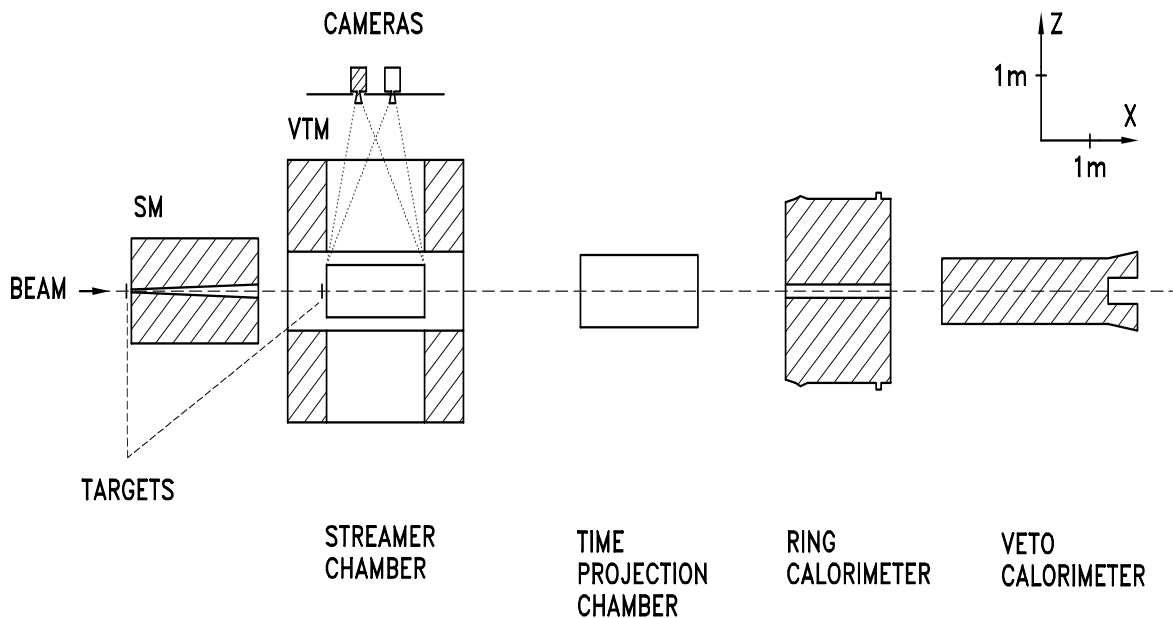

Figure 1. Experimental setup of experiment NA35 at the CERN SPS. The target is placed either in front of the streamer chamber (SETUP I and II) or in front of the sweeper magnet SM (SETUP III).

In order to measure forward-going strange particles and participant protons in the projectile hemisphere for the heaviest system (S+Au), the target and a sweeper magnet (SM) were installed upstream of the standard SETUP I configuration as shown in Fig. 1 (called SETUP III). The sweeper magnet has a vertical entrance opening of $\pm 2.5°$ for particles emerging from the target placed 6.3 cm upstream of this magnet. Due to its bending power of about 4.5 Tm all low momentum charged particles are swept out of the acceptance of the second magnet thus reducing the track density in the streamer chamber. This configuration not only enables measurement of strange particle decays in the projectile hemisphere but also covers participant protons beyond midrapidity ($y_{cm} = 3.0$) up to beam rapidity ($y_{proj} = 6.0$). This can be seen in Fig. 2 where the population of protons in transverse momentum p_T and rapidity y is presented. When sulphur projectiles are used the proton acceptance can be extended up to beam rapidity only in SETUP III.

A second large-volume tracking device, a time projection chamber with a sensitive volume of $240 \times 125 \times 112$ cm^3 [18] located downstream behind the analysing magnet was installed in 1990 and utilized in the ^{32}S–beam running for all three setups. It was also used in the deuteron–nucleus studies in the SETUP I configuration. The TPC detects

charged particles by measuring the ionisation of a particle, traversing the TPC, up to 60 times. For a primary track emerging from the production vertex the momentum of the particle can be calculated from the direction and position of the track inside the TPC. The TPC was positioned for most of the time such that it detected magnetically stiff negatively charged particles above midrapidity. The acceptance for negatively charged hadrons (pions) is illustrated in Fig. 3. Both tracking detectors combined cover almost all momentum space available for hadron production at SPS energy. In addition, the TPC identified charged particles by multiple sampling of the specific ionisation. This capability was used to measure antiproton spectra [19] and to distinguish electrons from negatively charged hadrons.
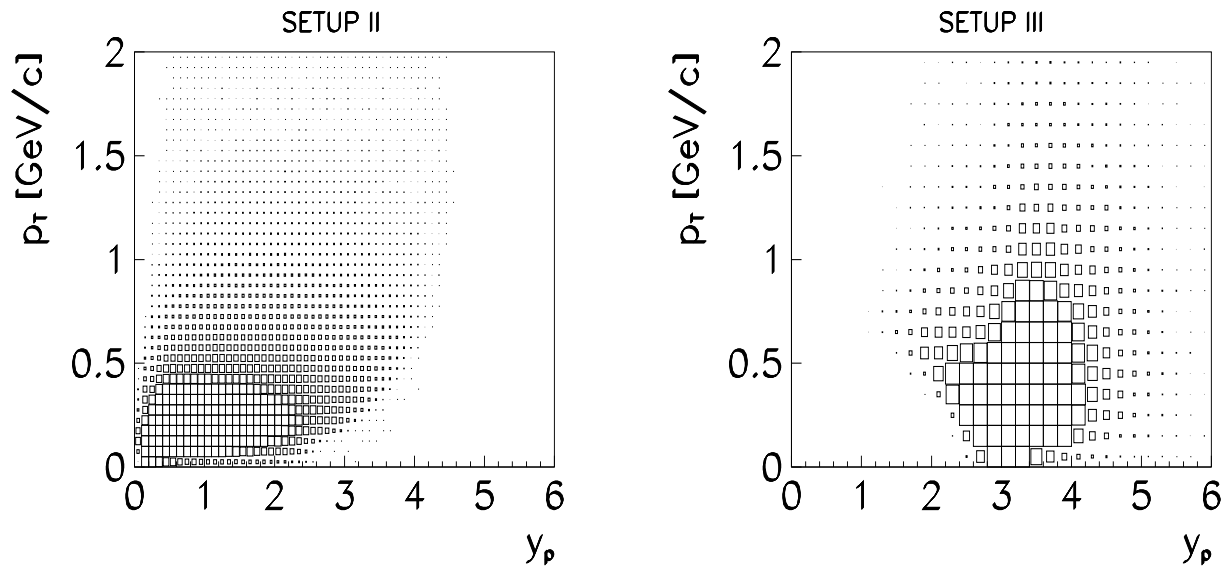
Figure 2. Acceptance of the streamer chamber in configuration SETUP II (left) and SETUP III (right) for protons, illustrated by the phase space population in a typical heavy ion collision. Note the forward acceptance of SETUP III.
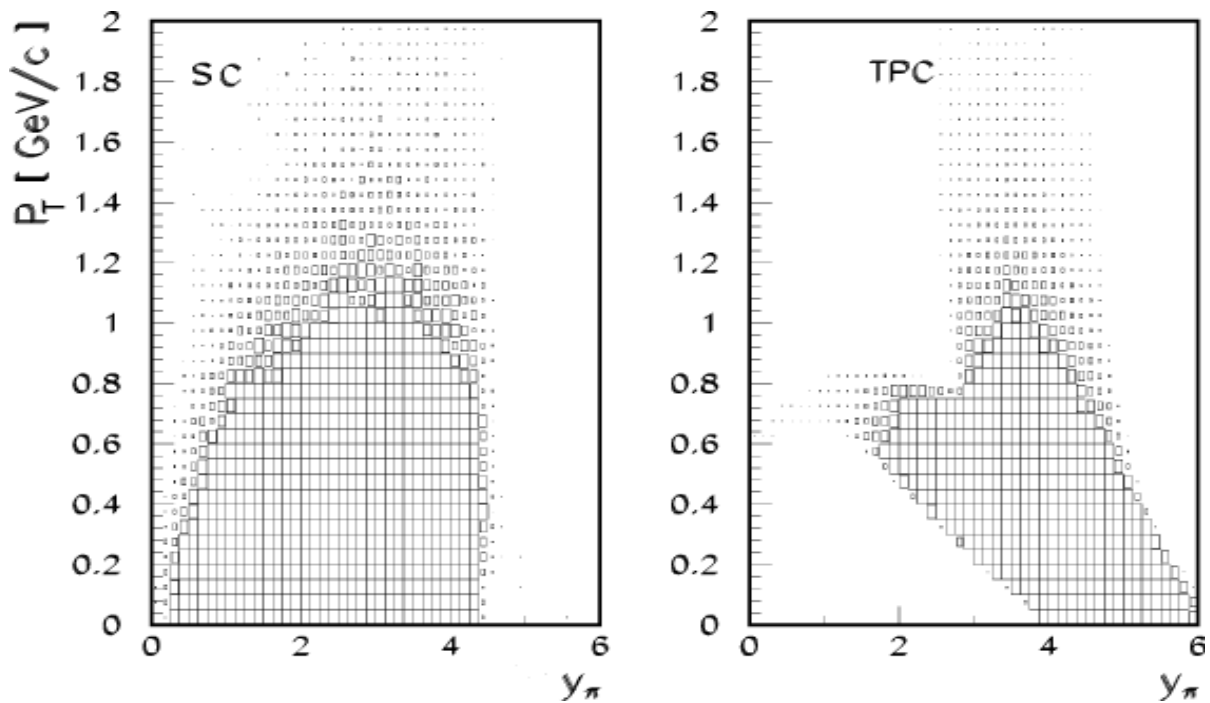

Figure 3. Acceptance of the two large-volume tracking detectors, the streamer chamber (left) and TPC (right) for SETUP II, illustrated by the phase-space population of negatively charged hadrons in a typical heavy ion collision.

3. Data sets

NA35 has studied a variety of collision systems, ranging from minimum bias proton–sulphur interactions to central sulphur–gold reactions. The central-collision fractions of the inelastic cross sections of the nucleus–nucleus collisions are typically the upper few percent of the inelastic cross section for the heavy ion induced reactions (see Table 1). Central events are selected either by a minimal energy deposition in the projectile fragmentation domain at forward angles ($\Theta_{lab} \leq 0.3°$) which is covered by the veto calorimeter (FET trigger), or by a large transverse energy deposition in the midrapidity calorimeters (TET trigger). In the case of p+S interactions a trigger was derived from a scintillation counter placed downstream of the streamer chamber which covered the projectile fragmentation domain. Its veto threshold was set just below the signal of the projectile particle and it selected essentially all inelastic interactions. An additional off-line selection of events with a charged particle multiplicity larger than five was applied in order to exclude contaminations due to non-target interactions in low multiplicity events.

Table 1
Characteristics of the data sets: colliding system, experimental configuration, number of events, trigger type, the selected fraction of the inelastic cross section, acceptance in rapidity for negatively charged hadrons and for protons. (The trigger for the d+Au interactions marked by (*) selects collisions where the deuteron projectile fully overlaps with the gold target.)

Reaction	Setup	Number of events	Trigger	$\frac{\sigma}{\sigma_{inel.}}$ [%]	Acceptance h^-	Acceptance protons
p+S	SETUP I		scint. veto $h^{+-} > 5$			
	internal target	735		63.5	$-2 \leq y_\pi \leq 4$	$-1 \leq y_p \leq 3$
	external target	339		63.5	$0.6 \leq y_\pi \leq 7$	$0.2 \leq y_p \leq 6$
p+Au	SETUP I	1603	FET	67	$0.6 \leq y_\pi \leq 6$	$0.2 \leq y_p \leq 6$
d+Au	SETUP I	2457	FET*	43	$0.4 \leq y_\pi \leq 6$	$0.2 \leq y_p \leq 6$
	TPC	9484	FET*	43	-	$2.8 \leq y_p \leq 4.4$
O+Au	SETUP I	565	FET	1.8	$0.6 \leq y_\pi \leq 3.8$	$0.2 \leq y_p \leq 3$
S+S	SETUP II	2650	FET	2.9	$0.6 \leq y_\pi \leq 3.8$	$0.2 \leq y_p \leq 3$
	TPC	23500	FET	3.5	$3.2 \leq y_\pi \leq 5.4$	-
S+Ag	SETUP II	13730	FET	3.2	$0.6 \leq y_\pi \leq 3.8$	$0.2 \leq y_p \leq 3$
	TPC	18000	FET	3.2	$3.2 \leq y_\pi \leq 5.4$	-
S+Au	SETUP I	331	TET	1.3	$0.8 \leq y_\pi \leq 3.6$	-
	SETUP III	3142	FET	6.3	$3.8 \leq y_\pi \leq 6.0$	$2.8 \leq y_p \leq 6$
	TPC	25700	FET	6.3	$3.2 \leq y_\pi \leq 5.4$	-

4. Data Analysis

The operation of the streamer chamber (SC) is described elsewhere [16, 17], the data analysis will briefly be described in the following. Streamer chamber pictures were scanned and measured using two different approaches: using the traditional film measurement by human operators or applying image processing and pattern recognition techniques to digitized streamer chamber data. Most of the streamer chamber data were analyzed automatically by the Frankfurt Image Processing System which is described in detail elsewhere [16]. The three perspective views of a streamer chamber event were recorded on 70 mm film and later digitized by a high resolution CCD-linescan camera. These digitized images were submitted to a series of image processing and pattern recognition programs. Tracks matched in the three stereoscopic views were then reconstructed in space. The particle momenta and the production vertex were obtained by fitting a trajectory to the measured points. The low multiplicity data obtained in SETUP I were analyzed on traditional projection tables by human operators.

Since the time projection chamber (TPC) was new to NA35 and relatively new for heavy ion applications [18], we will describe its operation briefly. A charged particle which traverses the sensitive volume of the TPC, ionizes gas molecules and produces electrons along its trajectory. Guided by a homogeneous electric drift field, the electrons drift towards the read-out MWPCs of the TPC. A field gradient at the sense wires leads to a multiplication of the drifted electrons by $5 \cdot 10^3$. The resulting space charge induces a signal onto the segmented cathode plane (pads). The centroid of these induced signals (clusters) can be determined with an accuracy of $\sigma = 500$ μm in pad direction and of $\sigma = 310$ μm in drift (time) direction. Pattern recognition is done by a simple track follower, which associates clusters with a straight line [20]. The particle momenta are determined by assuming that the particles emerge from a known production vertex.

4.1. Track recognition and reconstruction efficiency

The momentum resolution achieved with the streamer chamber as a continuous tracking device is approximately 3 MeV/c ($dp/p = 0.15\%$) for a typical pion with momentum of 2 GeV/c. The momenta in the TPC are typically higher than in the streamer chamber, since the TPC is located at more forward angles in the laboratory. The TPC resolution for 10 GeV/c tracks is approximately 1%.

In the streamer chamber track reconstruction losses due to tracks which overlap in the individual camera projections as well as to two-track resolution, pattern recognition and space reconstruction inefficiencies can be examined by either of two methods. The first method relies on human visual scanning of film data and multiple independent scans of the same data. The second method is a Monte Carlo simulation of digitally processed images. By this method heavy ion events are simulated using the FRITIOF event generator code [21]. The track trajectories are modeled through the NA35 experimental set-up using the GEANT detector simulation package [22]. For each track the streamers are calculated and then projected through the imaging system onto film. The film response and digitisation process are then simulated. The resulting digital event pictures are submitted to the

entire pattern recognition and track reconstruction process. This procedure provides the efficiency as a function of the two kinematical variables rapidity y and transverse momentum p_T. Both methods give an overall efficiency of about 95-97% for the highest multiplicities in our acceptance.

For the TPC the reconstruction efficiency was determined by a Monte-Carlo simulation using the VENUS event generator [12], the GEANT-program and a simulation of the TPC response [23]. The efficiency was found to be 90-95%, approximately independent of y and p_T within the geometrical acceptance. For the particle spectra the inefficiencies were corrected as a function of y and p_T.

A comparison of rapidity densities of negatively charged hadrons obtained by the streamer chamber analysis of SETUP II and SETUP III data and by the TPC analysis is shown in Fig. 4. For the symmetric system S+S streamer chamber data below midrapidity can be reflected about $y_{cm} = 3.0$ and then compared to TPC data above midrapidity as shown in Fig. 5. The TPC data below $y = 4.0$ and above $y = 4.6$ have been extrapolated to low and high p_T respectively by an exponential in $1/p_T \cdot dn/dp_T$. The comparisons in both figures demonstrate a satisfactory agreement (within several %).
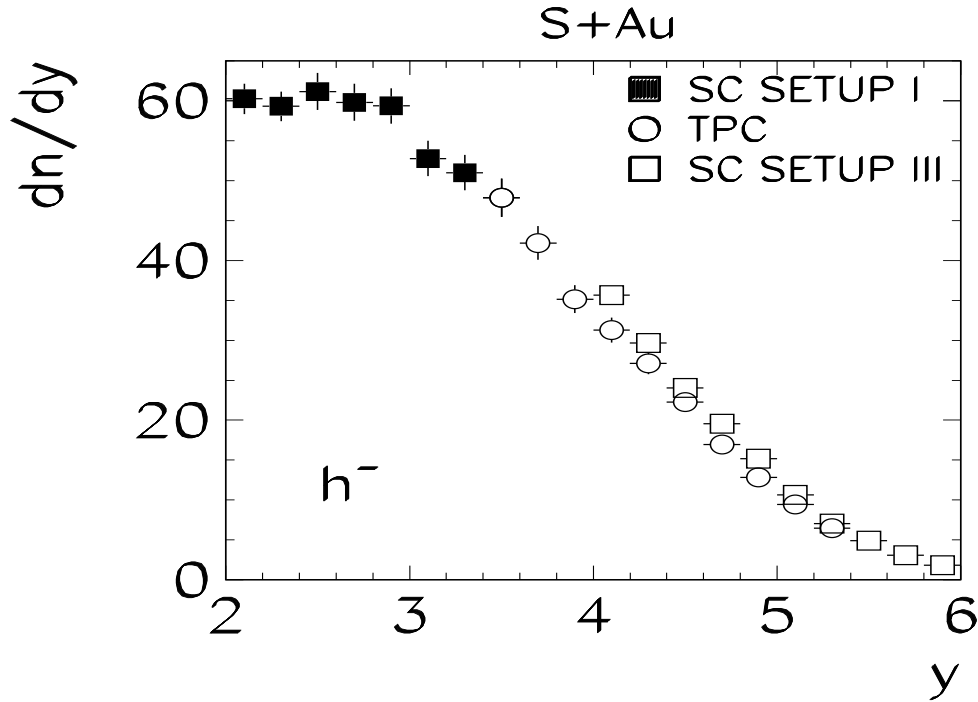

Figure 4. Rapidity distributions of negatively charged hadrons (pion mass assumed) produced in central S+Au collisions, measured in the streamer chamber (configurations SETUP I and SETUP III) and in the TPC.
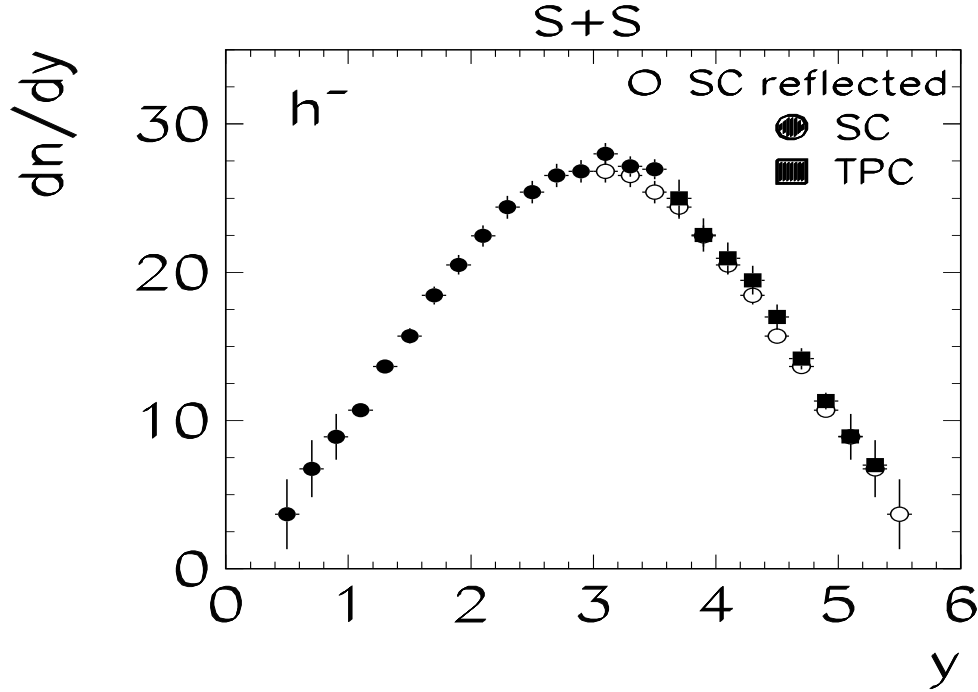
Figure 5. Rapidity distributions of negatively charged hadrons produced in central S+S collisions, measured in the streamer chamber (SETUP II) and reflected around $y_{cm} = 3$, and in the TPC.

4.2. Particle identification

We define negatively charged hadrons h^- as the sum of π^-, K^- and $\overline{p}$. Their average multiplicities in central S+S collisions are estimated to be about 90:7:1 [11, 19]. Corrections for electron contamination were made on a statistical basis (see next chapter). The rapidity of negatively charged hadrons was calculated assuming the pion mass, throughout; this implies that the K^- and $\overline{p}$ contributions to h^- rapidity distributions appear with an upward shift relative to their true position. A slight asymmetric widening of the rapidity distribution results. Since the streamer chamber has very little particle identification capability for stable particles, the net proton distribution was deduced from a measurement of the charge excess

$$\frac{dn}{dy}(AA' \to (p - \overline{p})) \approx \frac{dn}{dy}(AA' \to h^+) - \frac{dn}{dy}(AA' \to h^-),$$

where the rapidity is calculated assuming the proton mass. This is a good approximation for all rapidities in collisions of isoscalar nuclei (equal number of neutrons and protons) assuming local isospin conservation. Even for asymmetric systems deviations are expected to be small. Equating net protons to the charge-excess is subject to corrections which will be discussed below.

4.3. Corrections

All data in this paper are corrected for geometric acceptance and reconstruction inefficiencies, for e^+ and e^- misidentified as hadrons, for hadrons resulting from the weak decays of K_S^0, hyperons and for hadrons produced in secondary hadron-nucleus interactions.
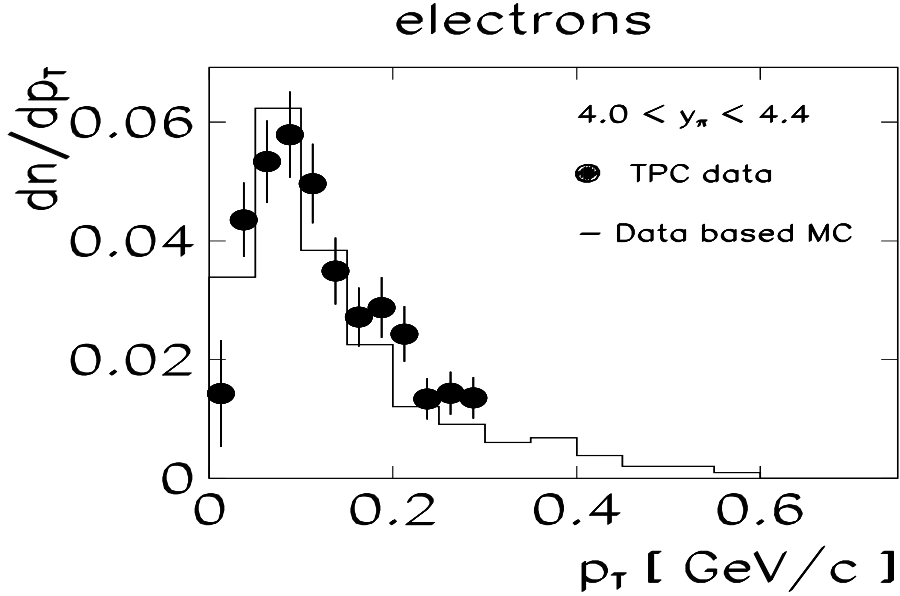

Figure 6. Transverse momentum spectrum of conversion electrons in central S+S collisions measured and identified in the TPC in the pion rapidity range $4.0 \leq y \leq 4.4$ compared to a calculated spectrum based on the measurement of negatively charged hadrons (see text for details). The vertical scale is given in $(\text{GeV/c})^{-1}$.

One source of contamination in the charged hadron spectra is the 2γ-decay of the abundantly produced π^0 inside the target and subsequent conversion of γs into e^+e^-–pairs. The spectral distributions of contaminant electrons were obtained from a Monte Carlo calculation using the experimental negative particle distributions and assuming equal π^0 and π^- meson multiplicities and spectra. An alternative method is to use the π^0 spectra obtained from an event generator (FRITIOF), with parameters tuned to reproduce the measured spectra, and a GEANT simulation for the subsequent decays and conversions. The latter method was employed at high rapidities, where the data based Monte Carlo may suffer from reconstruction inefficiencies at high momenta. The methods give similar results, which are confirmed by identified electron spectra that are measured in the TPC and displayed in Fig. 6. The electron contribution to the charged particle spectra is subtracted for each (y, p_T) bin.

The contamination of the negatively charged hadron spectra by pions produced in secondary interactions primarily in the target, and in weak decays is corrected for on the

basis of GEANT simulations (see e.g. [24]). The parameters of the event generators were tuned to reproduce the measured strange particle yields and spectra.

The contributions of the various contaminations as functions of p_T and y for a central S+Ag collision are shown in Figs. 7 and 8 respectively. The contaminations are largest at small p_T. The electrons dominate below transverse momenta of 150 MeV/c. The first p_T bin (50 MeV/c) especially is strongly affected by the electron correction, the amount of the contamination can be up to 50%. Above 150 MeV/c the weak decay products represent the main contamination to the spectrum. For larger transverse momenta the various contributions get smaller. The rapidity dependence of the decay product contamination follows the distribution of the primaries, while electrons and secondary interactions contribute more strongly at low rapidities (Fig. 8). The overall systematic error on the spectra is estimated to be less than 5% for p_T above 50 MeV/c.

All data - spectra of both negatively and positively charged hadrons - were corrected as described above. In addition, when deriving the net proton spectra from the charge excess, a correction is applied for the excess of the K^+ relative to the K^- yield. Since these corrections are based on measurements of the same experiment over a wide acceptance, the corrections are model independent. Nevertheless, these corrections become large at low transverse momenta, particularly at low rapidities, and therefore a low-p_T cut was applied to the net proton spectra. This cut also takes care of possible differences in the π^+ and π^- yields for non-isoscalar systems of colliding nuclei. In order to obtain rapidity densities the transverse momentum spectrum was extrapolated into the part below the cut using a thermal fit to the data. This extrapolation contributes approximately 20% (assuming a temperature of about 200 MeV and a p_T-cut of 300 MeV/c) to the cross section.

The validity of equating participant protons to the charge-excess even in asymmetric systems is demonstrated in Fig. 9. Particles taken from a simulation (FRITIOF) were passed to a GEANT-program of the experimental setup. After all corrections described above the net proton distribution which was deduced from the charge excess agrees very well with the input distribution of net protons within the acceptance $0.2 < y < 3.0$. The overall systematic error on the participant proton spectra is estimated to be less than 12%. Note that this conclusion does not rest on the implication that the FRITIOF prediction in Fig. 9 gives a good account of the data (see sect. 6.1.3).
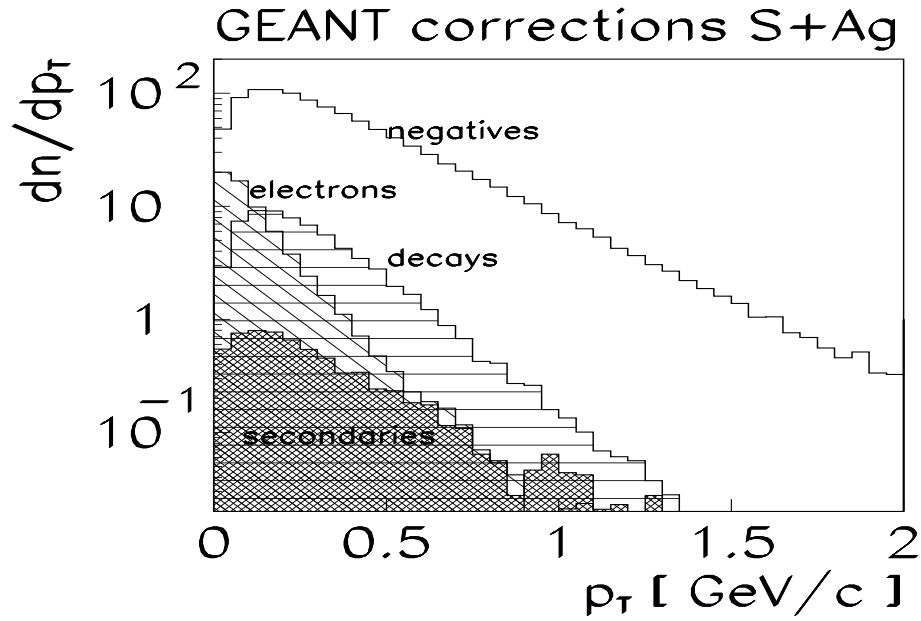
Figure 7. Composition of a measured transverse momentum spectrum of negatively charged particles, based on a tuned event generator (FRITIOF) and a GEANT simulation. The vertical scale is given in $(\mathrm{GeV}/c)^{-1}$.
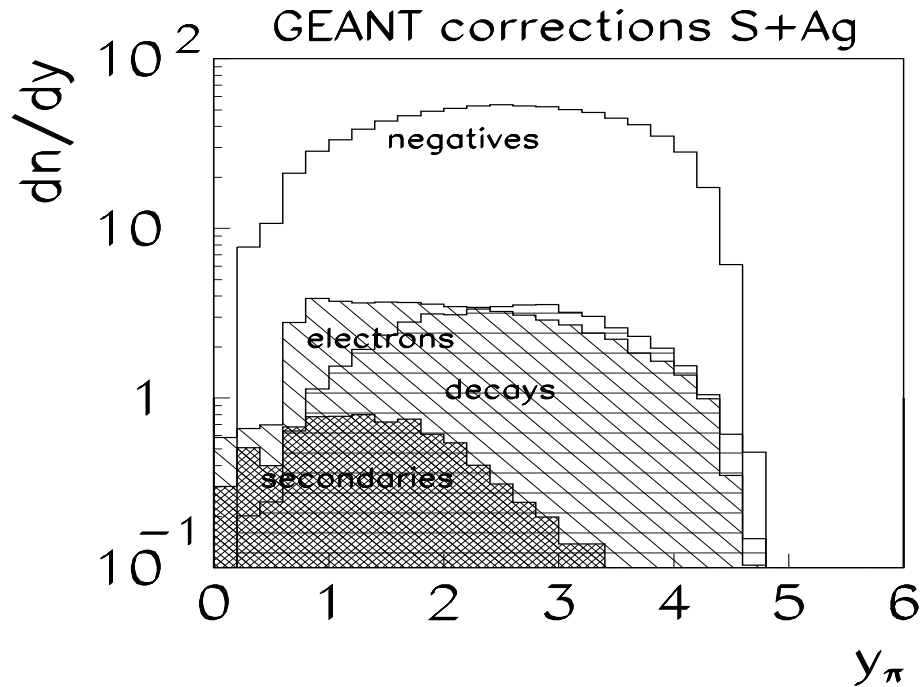

Figure 8. Composition of a measured rapidity spectrum of negatively charged particles, based on a tuned event generator (FRITIOF) and a GEANT simulation.
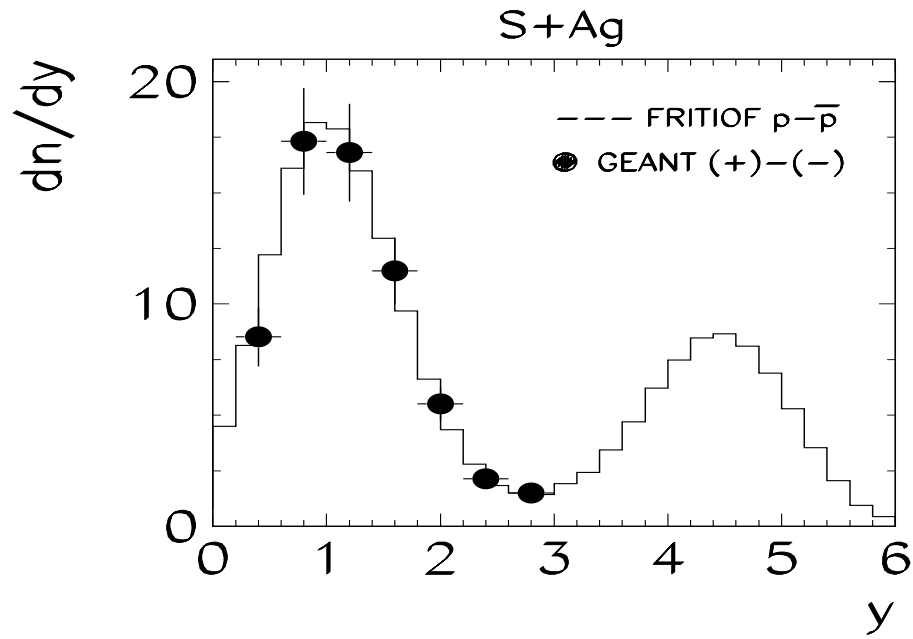
Figure 9. Simulated rapidity distributions of net protons $(p - \overline{p})$ and of reconstructed net protons deduced from the charge excess after all corrections for central S+Ag collisions.

5. Net Baryons

In a simple picture of high energy nucleus–nucleus collisions one distinguishes two classes of nucleons: spectators and participants. Spectator nucleons are defined as those which did not suffer collisions and therefore have their momenta located inside the Fermi spheres of the interacting nuclei. Participant nucleons are those which suffer collisions that affect their momentum sufficiently to remove them from the Fermi sphere of the incoming nuclei. Some of them may be converted into strange and multistrange baryons. Integrating the rapidity distributions of net baryons (baryons minus antibaryons) between $y = 0.2$ and $y = 5.8$ yields an estimate of the total number of participant baryons. This estimate is only accurate in the case of central collisions of identical nuclei (S+S), where the number of spectators is small compared to the number of participants so that the result of the technical procedure to separate spectators and participants depends only weakly on the cuts used. For asymmetric systems the net baryon number as calculated in this paper should be treated as a crude approximation of the number of participants since cascading processes in the target spectator matter may invalidate the definition of a spectator.

5.1. Rapidity distributions

Rapidity distributions of net protons were obtained from the charge excess with the associated corrections discussed above. Since these corrections become large at low transverse momenta, a cut was applied at 300 MeV/c (for S+A collisions at 400 MeV/c). The missing low momentum part was extrapolated on the basis of a thermal fit in order to obtain rapidity densities (see chapter 5.2). In comparing rapidity distributions for the various systems one has to keep in mind that different forward energy triggers may affect the spectra differently.

5.1.1. Proton-Nucleus Collisions

The rapidity distributions of net protons for minimum bias p+S and p+Au interactions are shown in Fig. 10. While the rapidity densities around midrapidity ($y_{cm} = 3$) for both reactions are not very different, clear differences are observed for rapidities below 1.2 and larger than 4.4. In p+Au collisions more target nucleons participate in the reactions and are therefore shifted up to one unit in rapidity farther than in p+S collisions. For the projectile the gold nucleus looks black, i.e. the probability of the projectile to traverse the target nucleus without losing any or little energy is small. For p+S interactions on the other hand, one can perceive a clear projectile proton peak at rapidity ≈ 4.7.
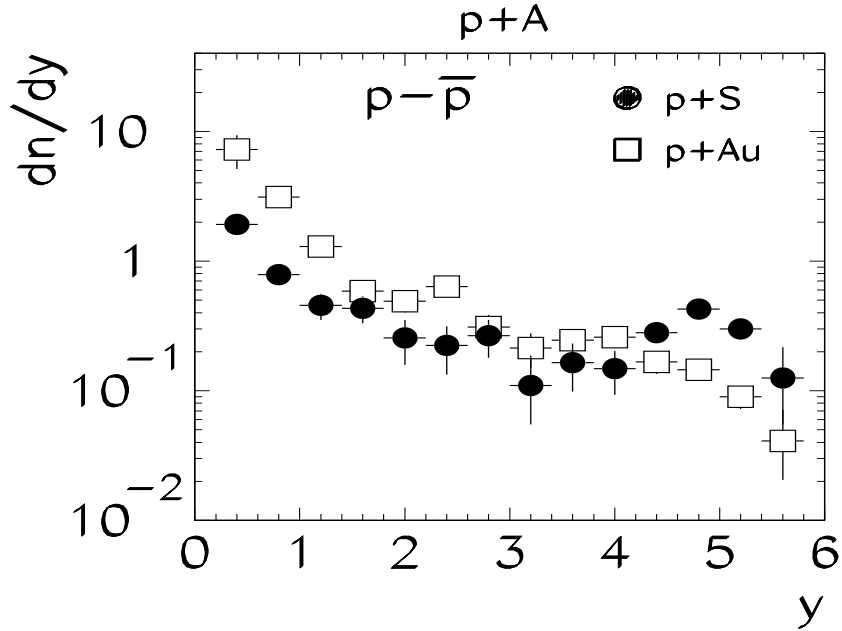
Figure 10. Rapidity distributions of net protons $(p - \overline{p})$ for minimum bias p+S and p+Au collisions at 200 GeV/nucleon.

5.1.2. Nucleus-Gold Collisions

In order to study the dependence of nuclear stopping on the mass of the projectile in the case of incidence on a heavy target nucleus, net proton rapidity distributions were measured for various 'full overlap' collisions: central d+Au, central O+Au and central S+Au reactions. These data are displayed in Fig. 11. O+Au collisions were measured in the streamer chamber for rapidities below midrapidity, $y < y_{cm}$, SETUP I. The S+Au data were measured in the streamer chamber configuration SETUP III at rapidities $y > y_{cm}$. The rapidity density at midrapidity, $y = y_{cm}$, is observed to increase with projectile mass. A comparison of the rapidity distribution for S+Au collisions with the distributions for d+Au and O+Au, multiplied by 16 and 2 (the inverse ratios of the projectile nucleons relative to the S+Au reaction), respectively, is displayed in Fig. 12. For the O+Au data at a beam energy of 60 GeV/nucleon the rapidity axis is scaled by the ratio of the beam rapidities $(y_{proj}$ (200 GeV/nucleon) / y_{proj} (60 GeV/nucleon) = 6.0/4.8) prior to plotting in Fig. 12 [25, 26]. The resultant rapidity distributions are similar for $y > y_{cm}$. This implies that the stopping of projectile nucleons is rather independent of the size of the projectile nucleus and its energy in collisions with a heavy target nucleus.
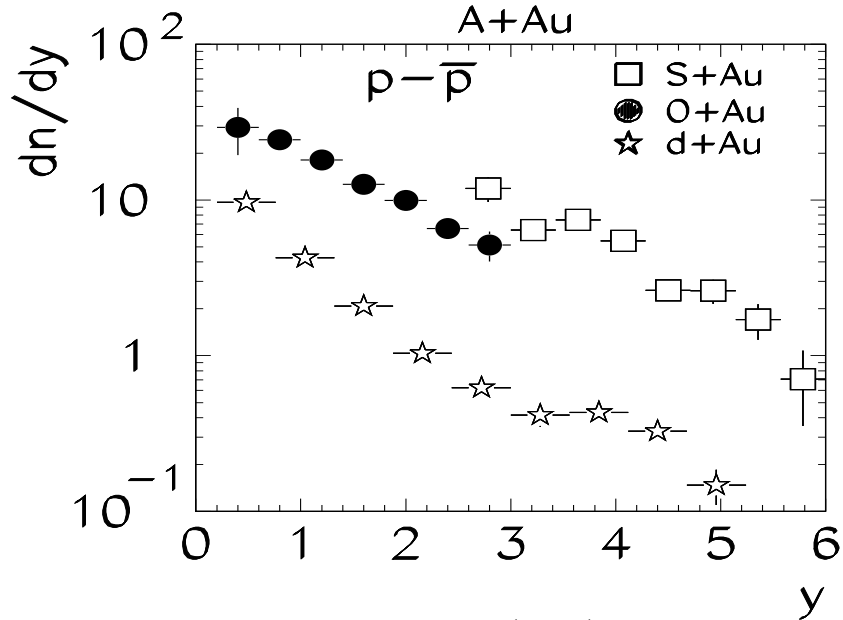
Figure 11. Rapidity distributions of net protons $(p - \overline{p})$ for central d+Au, central O+Au and central S+Au collisions at 200 GeV/nucleon.
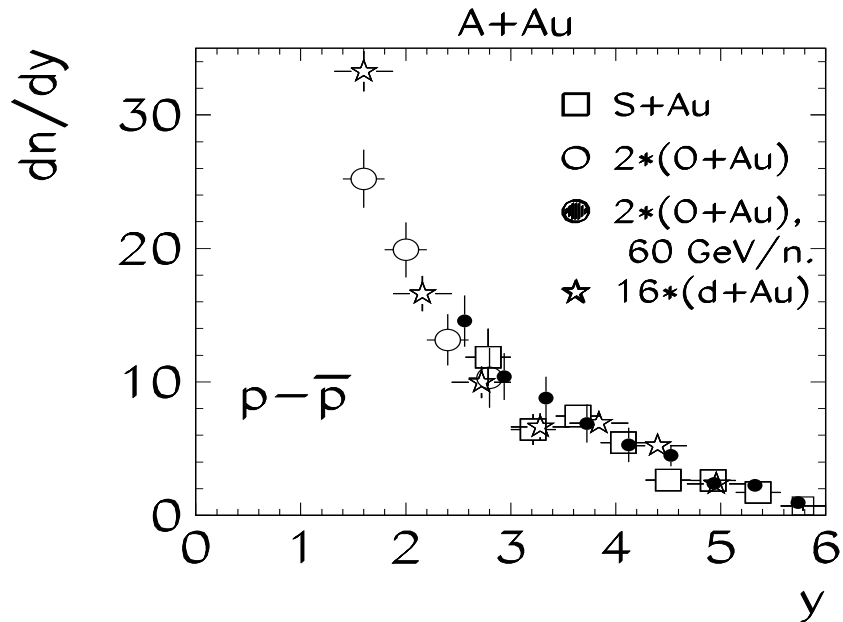

Figure 12. Scaled rapidity distributions of net protons for central $16 \cdot$(d+Au), central $2 \cdot$(O+Au) and central S+Au collisions. For the case of the 60 GeV/nucleon data the rapidities are scaled by the ratio of the beam rapidity relative to that of 200 GeV/nucleon.

5.1.3. Sulphur-Nucleus Collisions

To investigate the effect of changing the nuclear thickness of the target, rapidity distributions of net protons were measured for central S+S, S+Ag and S+Au collisions. The data are shown in Fig. 13. The S+S and S+Ag data were measured in the SETUP II for $y < y_{cm}$ and S+Au data in the SETUP III for $y > y_{cm}$. For the symmetric system S+S, the data points reflected at y_{cm} are also shown. The shape of the net proton rapidity distribution changes from being relatively flat for the light symmetric system (S+S) to a monotonic decrease with rapidity for the asymmetric systems. The rapidity density at $y = y_{cm}$ increases for heavier projectiles, and is a factor of about two larger for S+Au relative to S+S collisions. There is an excess of net protons in the forward direction for the lighter S+S reaction relative to the S+Au reaction. Thus, it is evident that the S target nucleus is less effective than the Au nucleus in stopping (slowing down) incident projectile nucleons. For the S+Au system, projectile protons are shifted further backward in rapidity than for the S+S system. The rapidity densities near midrapidity agree with the values obtained by the NA44 experiment for identified protons and antiprotons as shown in Table 2.
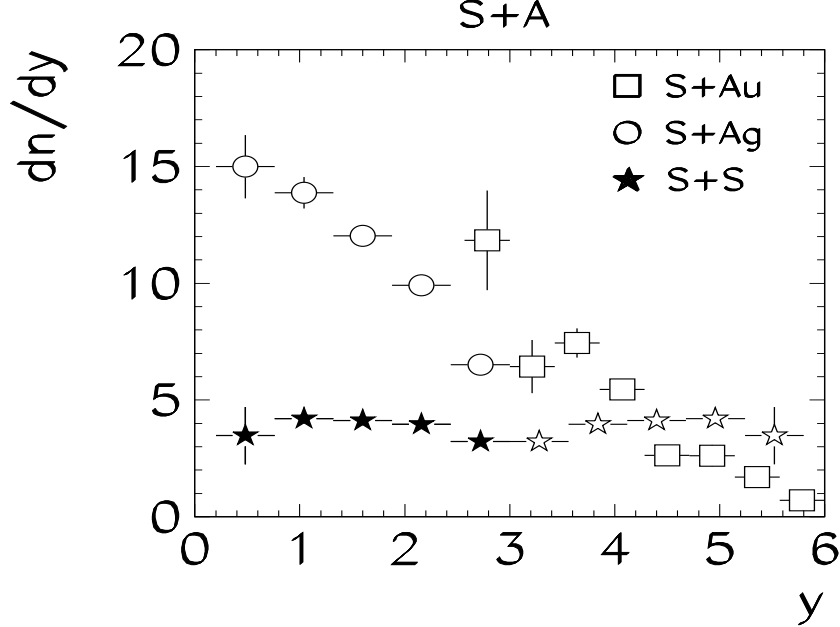

Figure 13. Rapidity distributions of net protons $(p - \bar{p})$ for various central S–nucleus collisions at 200 GeV/nucleon.

5.1.4. Rapidity Shift

Before the collision the nucleon rapidity distribution is concentrated in peaks at the target rapidity $y = 0$ and at beam rapidity $y = y_{proj}$, with the peak width given by the Fermi momentum inside the nuclei ($\Delta y \approx 0.2$). After the collision, target and projectile nucleons are shifted towards midrapidity, with some nucleons converted into (multi)strange

Table 2

Rapidity densities of net protons $(p - \overline{p})$ near midrapidity $(y \approx 2.8)$ in central S+S and S+Au(Pb) collisions [27].

	$dn/dy \ (p - \overline{p})$	
Reaction	this paper	NA44 [27]
S+S	3.2 ± 0.4	3.2 ± 1.5
S+Au(Pb)	12 ± 2	12.4 ± 2.1

baryons. The latter must also be counted in the evaluation of rapidity loss. The rapidity distributions of net hyperons $(\Lambda - \overline{\Lambda})$ for minimum bias p+S and p+Au collisions are displayed in Fig. 14. Those for central collisions of S+S, S+Ag, and S+Au are displayed in Fig. 15. The trends in the rapidity distributions for net hyperons as a function of target nucleus are similar to those for net protons described in the previous section.

In order to quantify the amount of stopping in symmetric and asymmetric collisions, the average rapidity loss (or mean rapidity shift) $\langle \delta y \rangle = y_{proj} - \langle y \rangle$ is defined, where y_{proj} is the incoming projectile rapidity and $\langle y \rangle$ is the average net baryon rapidity after the collision. For symmetric systems the average rapidity was calculated by averaging the rapidity of the net protons in the interval from $y_{cm} = 3$ to $y_{proj} - 0.2$. For the asymmetric systems $\langle y \rangle$ is defined as the average rapidity of the net proton dn/dy distribution in the projectile hemisphere from $y_{proj} - 0.2$ to a rapidity such that the integral under the distribution equals the number of net projectile protons [28]. If the target and projectile nucleons mix, the rapidity loss defined in this manner is a lower limit.

The average rapidity losses $\langle \delta y \rangle$ for collisions of various projectiles with sulphur and gold targets are displayed in Fig. 16. For each target $\langle \delta y \rangle$ is approximately independent of projectile mass (but may also be construed as being consistent with a slight increase with projectile mass). The most obvious trend is a shift from $\langle \delta y \rangle = 1.2$ - 1.6 for sulphur target interactions to $\langle \delta y \rangle = 2.0$ - 2.3 for the gold target interactions.
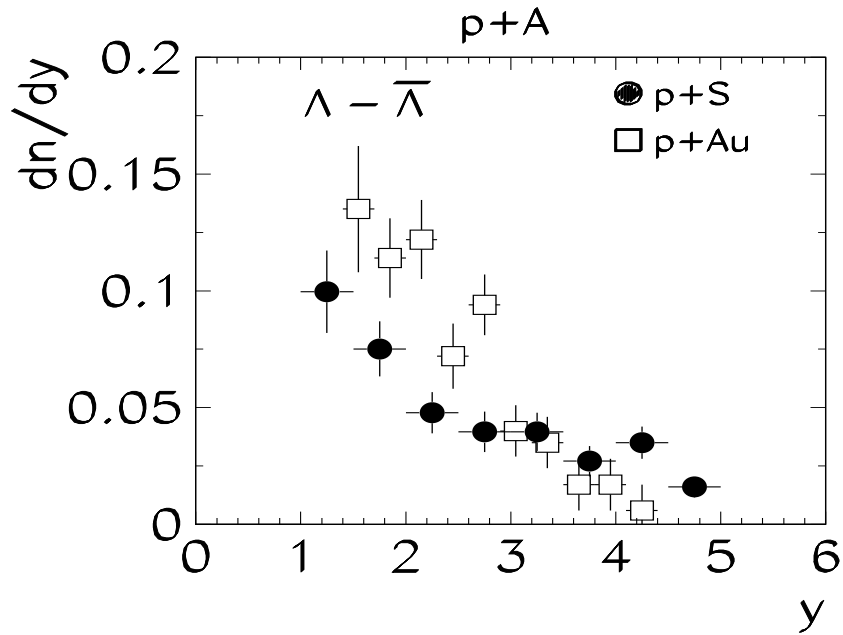
Figure 14. Rapidity distributions of net hyperons ($\Lambda - \overline{\Lambda}$) for minimum bias p+S ($1.0 < y < 5.0$) and p+Au ($1.4 < y < 4.4$) collisions at 200 GeV/nucleon.
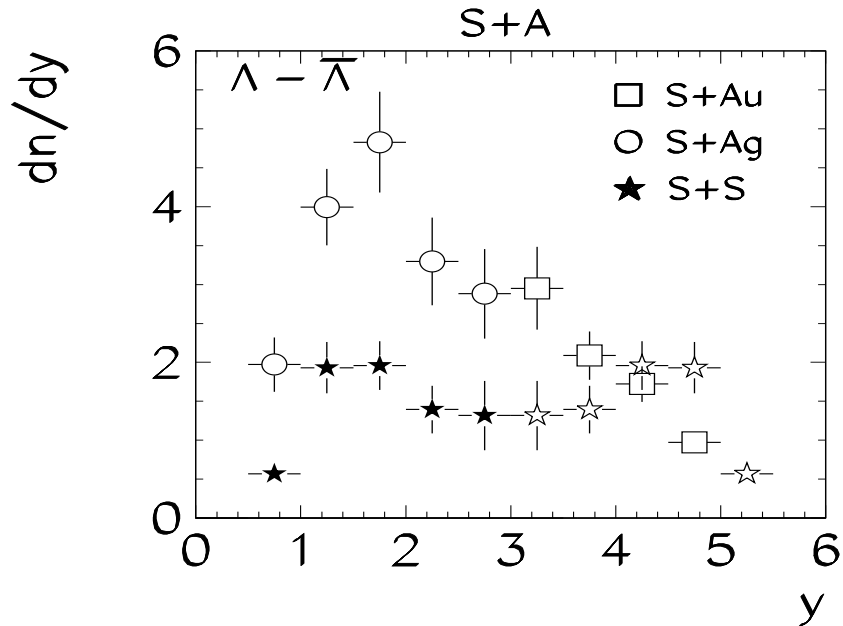

Figure 15. Rapidity distributions of net hyperons ($\Lambda - \overline{\Lambda}$) for central S+S ($0.5 < y < 3.0$), S+Ag ($0.5 < y < 3.0$) and S+Au ($3.0 < y < 5.0$) collisions at 200 GeV/nucleon. The solid stars are measured S+S data, the open stars are reflected at $y = y_{cm}$.
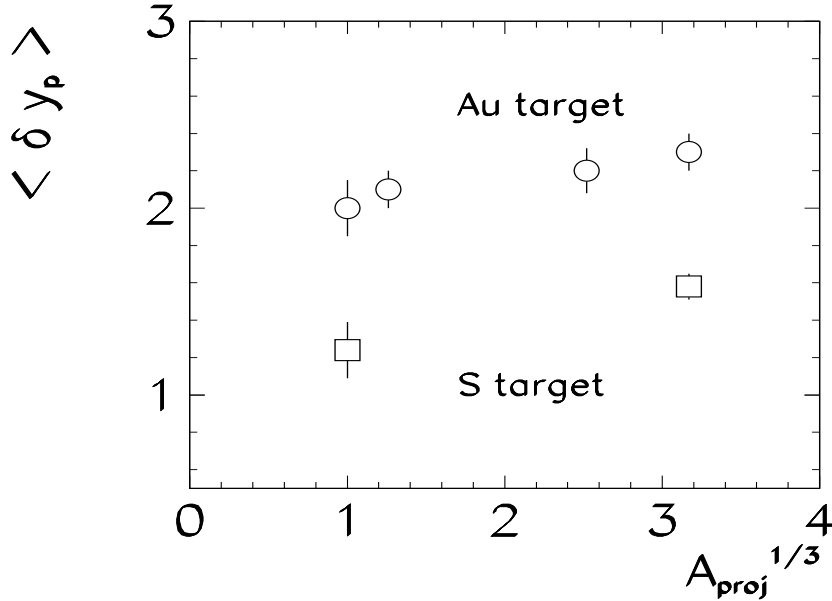
Figure 16. Average rapidity loss (mean rapidity shift) of net projectile protons for various projectiles incident on sulphur and gold targets at 200 GeV per nucleon.

5.1.5. Number of Net Baryons

By integrating the rapidity distributions the number of net protons inside the acceptance was obtained and is shown in Table 3. The total number of net protons is defined as the net proton number in the final state outside the 'Fermi spheres' of the projectile and target nuclei - approximated by selecting a rapidity range 0.2 to 5.8. For systems where the acceptance does not cover the rapidity range from 0.2 to 5.8, we extrapolated the rapidity distribution. For the O+Au data the extrapolation was based on the observed scaling behaviour of 60 GeV/nucleon O+Au data (see section 5.1.2). The number of net protons in S+Ag collisions at $3.0 \leq y \leq 5.8$ was estimated to be the average of S+S and S+Au data.

The charge-excess method, corrected for the K^+/K^- asymmetry and strange hyperon decays, leads to the number of *observed* net protons. In order to estimate the total number of net baryons one needs in addition an estimate of the total number of net hyperons. Table 4 shows the measured yields of net lambdas $(\Lambda - \overline{\Lambda})$ measured in the same experiment [8, 9, 10]. We derived the corresponding correction for the total number of net hyperons from the $(\Lambda - \overline{\Lambda})$ distributions using Wróblewski's empirical rule [29] $N_Y = 1.6 \cdot N_\Lambda$.

Multiplying the number of net protons by 2 (in the case of p-induced reactions only in the target hemisphere) and adding the corrected number of hyperons gives an estimate of the total number of net baryons. These estimates are shown in Table 5. This procedure is valid for collisions of *isoscalar* nuclei (equal number of neutrons and protons) and only a crude approximation in all other cases. Only in the case of central collisions of

isoscalar nuclei the number of net baryons equates the number of participant nucleons. Comparing the measured number of net baryons with the number of wounded nucleons using the standard geometrical approach [30] one finds a discrepancy between these two numbers in asymmetric systems. This can be explained by target spectators misidentified as participants or additional participants due to cascading effects in spectator matter.

Table 3
Number of observed net protons $(p-\overline{p})$ in p-nucleus, central deuteron-nucleus and central nucleus-nucleus collisions. The values in italics are the result of an extrapolation. See text for details.

	$p - \overline{p}$		
Reaction	$0.2 \leq y \leq 3.0$	$3.0 \leq y \leq 5.8$	$0.2 \leq y \leq 5.8$
p+S	-	-	2.4 ± 0.2
p+Au	-	-	5.9 ± 0.2
d+Au	-	-	10.7 ± 0.2
O+Au	42 ± 5	-	*47 ± 5*
S+S	10.6 ± 0.8	10.6 ± 0.8	21.2 ± 1.3
S+Ag	32 ± 2	-	*43 ± 3*
S+Au	-	11.4 ± 0.5	-

Table 4
Number of observed net lambdas $(\Lambda - \overline{\Lambda})$ in p-nucleus and central nucleus-nucleus collisions. The values in italics are the result of an extrapolation. See text for details.

	$\Lambda - \overline{\Lambda}$		
Reaction	$1.0 \leq y \leq 5.0$	$1.4 \leq y \leq 4.4$	$0.2 \leq y \leq 5.8$
p+S	0.19 ± 0.02	-	*0.23 ± 0.03*
p+Au	-	0.20 ± 0.02	*0.28 ± 0.03*
	$0.5 \leq y \leq 3.0$	$3.0 \leq y \leq 5.5$	$0.2 \leq y \leq 5.8$
S+S	3.6 ± 0.4	3.6 ± 0.4	*7.2 ± 0.6*
S+Ag	8.5 ± 0.8	*3.9 ± 0.5*	*12.6 ± 1.2*
		$3.0 \leq y \leq 5.0$	
S+Au	-	3.9 ± 0.4	-

Table 5

Estimated total number of net baryons $< B - \overline{B} >$ in p-nucleus and central nucleus-nucleus collisions compared to the number of wounded nucleons $< W >$ (the values for p+S and p+Au marked by (*) are averaged over all impact parameters).

Reaction	$< B - \overline{B} >$ $0.2 \leq y \leq 5.8$	$< W >$ calculated
p+S	4.2 ± 0.8	3.2^*
p+Au	-	4.7^*
d+Au	-	10
O+Au	-	68
S+S	54 ± 3	53
S+Ag	105 ± 12	92
S+Au	-	113

5.2. Transverse momentum distributions of net protons

The invariant cross sections as a function of the transverse momentum for net protons are compatible with the following parametrization of the transverse momentum spectra as suggested by thermodynamic models:

$$\frac{1}{p_T}\frac{dn}{dp_T} = C \cdot m_T \cdot K_1(\frac{m_T}{T_1}),\tag{1}$$

where $m_T = \sqrt{p_T^2 + m_0^2}$ is the transverse mass of particles with rest mass m_0, C is a normalization factor and K_1 is the modified Bessel function of order one. The parameter T_1 is determined by fitting the experimental data and can be interpreted in thermal models without transverse flow as the thermal freeze-out 'temperature'.

Figs. 17-19 show transverse momentum distributions of net protons for various collision systems at 200 GeV/nucleon together with fits to Eq. 1. The invariant spectra of protons as a function of p_T for various systems are well described by inverse slope parameters ('temperatures') of approximately 200 MeV (Table 6). The 'temperatures' are observed to increase with the mass of the colliding system and are highest at midrapidity. The 'temperatures' range from $T \approx 145$ MeV for minimum bias p+S to $T \approx 220 - 240$ MeV for central collisions of S+S, S+Ag and S+Au. Dividing the rapidity range into two bins, $0.5 \leq y \leq 2.0$ and $2.0 \leq y \leq 3.0$, and fitting the spectra separately in these bins results in inverse slope parameters that are about 40 MeV higher at midrapidity as compared to the values at lower rapidity for all systems.
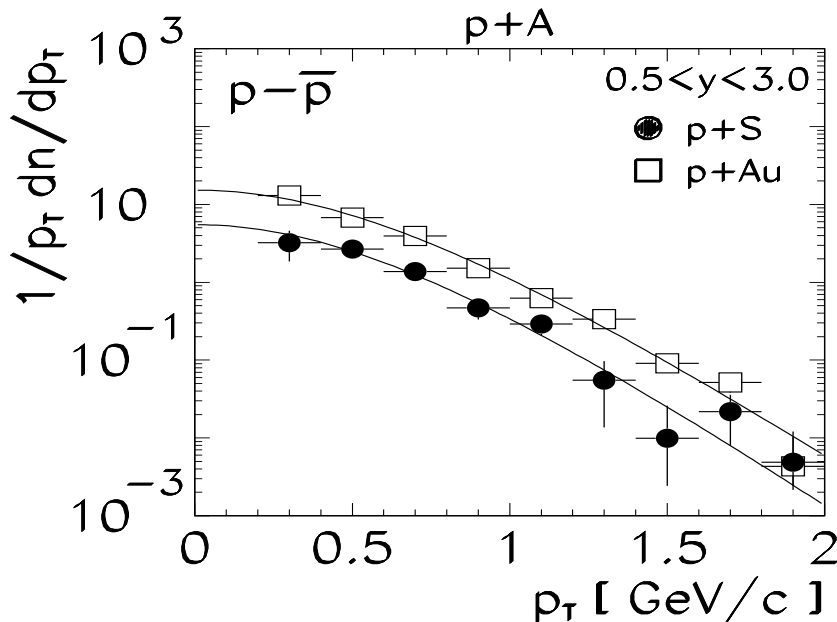

Figure 17. Transverse momentum distributions of net protons for minimum bias p+S and p+Au collisions. The vertical scale is given in $(\text{GeV})^{-2}$.
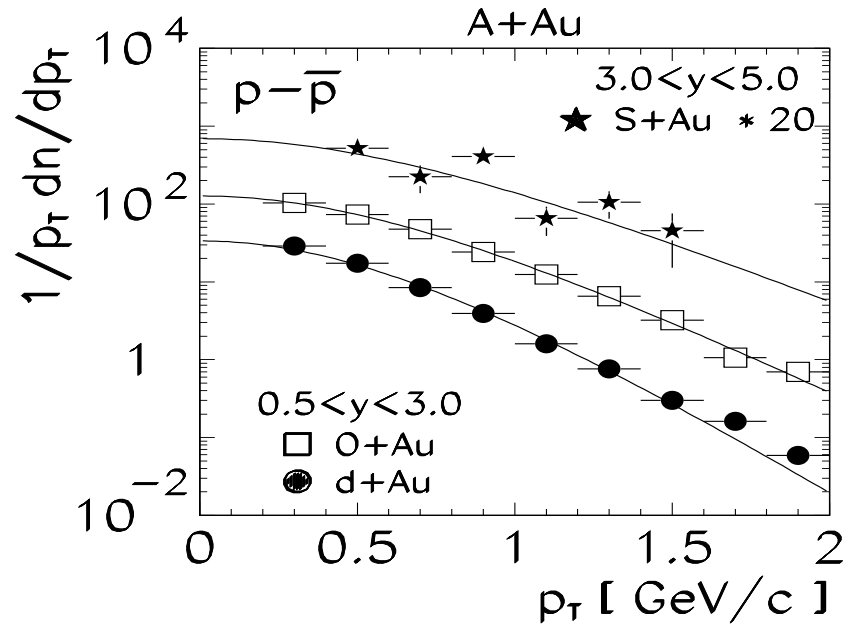
Figure 18. Transverse momentum distributions of net protons for central d+Au, O+Au and S+Au collisions. The vertical scale is given in $(GeV)^{-2}$.
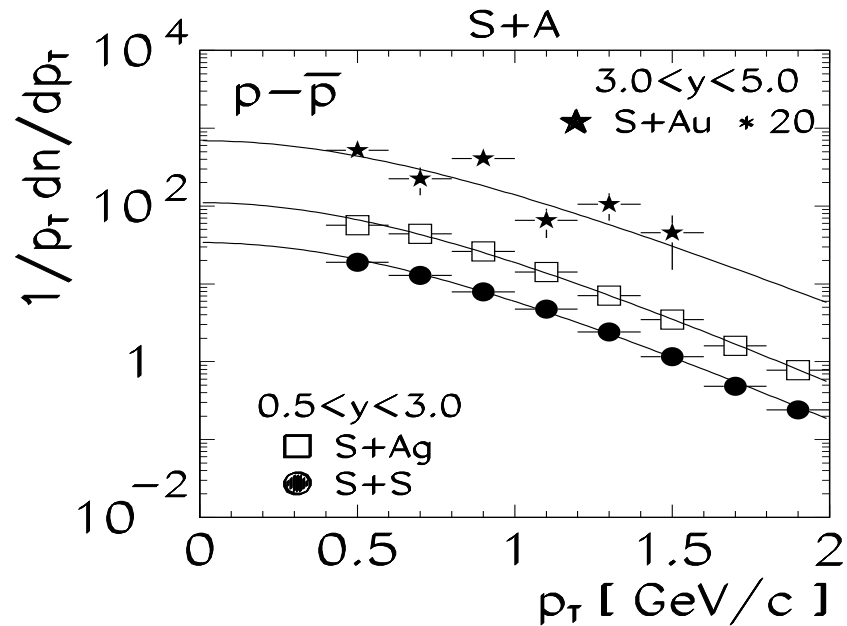

Figure 19. Transverse momentum distributions of net protons for central S+S, S+Ag and S+Au collisions. The vertical scale is given in $(GeV)^{-2}$.

Fitting a simple exponential

$$\frac{1}{p_T} \frac{dn}{dp_T} = C \cdot \exp\left(-\frac{m_T}{T_2}\right) \tag{2}$$

results in somewhat higher 'temperatures' as shown in Table 6. Also shown are our pub-lished results for S+S collisions and results from another experiment. The 'temperature' reported by NA35 in [3] was about 40 MeV lower. Much higher statistics of the recent data allowed a more detailed contamination correction as described in Section 4. NA44 data [27, 31] measured in a small rapidity interval near midrapidity for less central collisions yield somewhat lower inverse slope parameters.

Table 6
'Temperatures' obtained from thermal fits (Eq. 1) and fits according to Eq. 2 to the trans-verse momentum distributions of participant protons in various collisions. The systematic error is about 10 MeV.

	T_1 [MeV] (Eq. 1)		T_2 [MeV] (Eq. 2)	
Reaction	$0.5 \leq y \leq 3.0$	NA35	$0.5 \leq y \leq 3.0$	NA44
p+S	145 ± 11		154 ± 14	
p+Au	156 ± 4		163 ± 5	
d+Au	161 ± 2		172 ± 5	
O+Au	204 ± 4		219 ± 5	
S+S	226 ± 5	180 ± 14 [3]	235 ± 9	208 ± 8 [31]
S+Ag	224 ± 2		238 ± 2	
	$3.0 \leq y \leq 5.0$		$3.0 \leq y \leq 5.0$	
S+Au	244 ± 43		276 ± 48	242 ± 3 [27]

6. Negatively Charged Hadron Production

Essentially all of the energy deposited in the reaction volume by the participant nucleons goes into the production of hadrons. Without extensive particle identification in this experiment, only distributions of inclusive charged hadrons can be measured and separation of various species (such as π^+, K^+, p) is not possible. The positive hadron distributions are more complicated to interpret than the negative ones, since the contribution of K^+ and p is a large contamination. Thus, we will concentrate on the distributions of negative hadrons which are primarily π^- mesons. The relevant contamination and acceptance corrections as described in section 4 were applied.

6.1. Rapidity Distributions
6.1.1. Proton-Nucleus Collisions

The rapidity distributions of negatively charged hadrons produced in p+S and p+Au interactions are shown in Fig. 20. For comparison nucleon–nucleon reactions are also included. The nucleon–nucleon interactions are defined here as $0.5 \cdot [(p+p \rightarrow \pi^+) + (p+p \rightarrow \pi^-)]$, the data are taken from [33] (cf. [34] and [35] and references therein). The h^- from nucleon–nucleon interactions peak at midrapidity. The multiplicity increases with target mass, and the maximum of the distribution shifts to lower rapidities with increasing target mass. This is indicative of π^--production after multiple collisions. For $y \geq 4$, the yield of h^- produced in p+Au collisions appears to be lower than that for nucleon–nucleon and p+S collisions. Fig. 21 shows a comparison to minimum bias p+p, p+Ar and p+Xe data from experiment NA5 at the CERN-SPS [36].
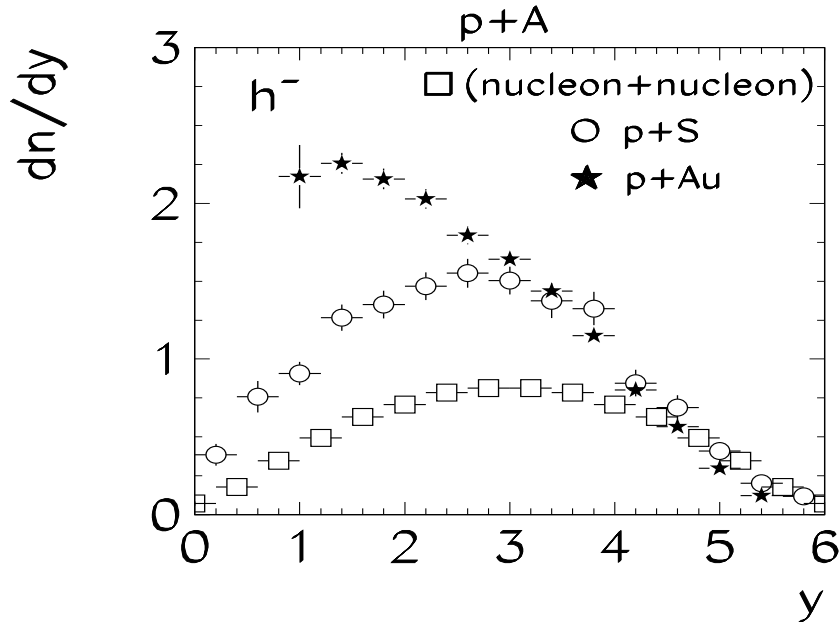

Figure 20. Rapidity distributions of negatively charged hadrons produced in minimum bias nucleon–nucleon, p+S and p+Au collisions.
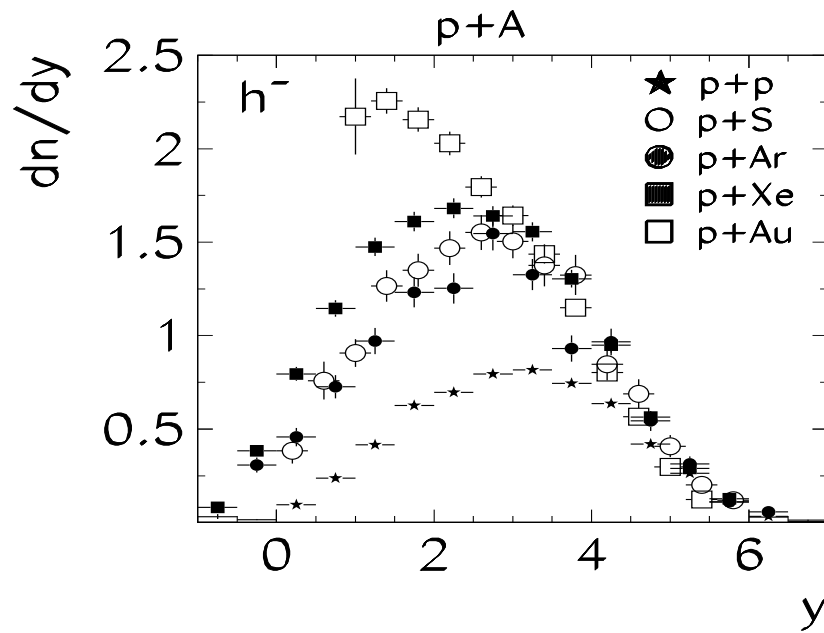
Figure 21. Rapidity distributions of negatively charged hadrons produced in minimum bias p+p, p+S, p+Ar, p+Xe and p+Au collisions [36]. Note that the rapidity distribution for p+S collisions is higher than for p+Ar interactions due to different trigger conditions and event selections.

6.1.2. Nucleus-Gold Collisions

The rapidity distributions of negatively charged hadrons produced in central d+Au, O+Au and S+Au collisions are shown in Fig. 22. The distributions exhibit a peak at y below $y_{cm} = 3$. The multiplicity increases with projectile mass, and the maximum of the distribution moves toward midrapidity with increasing projectile mass.
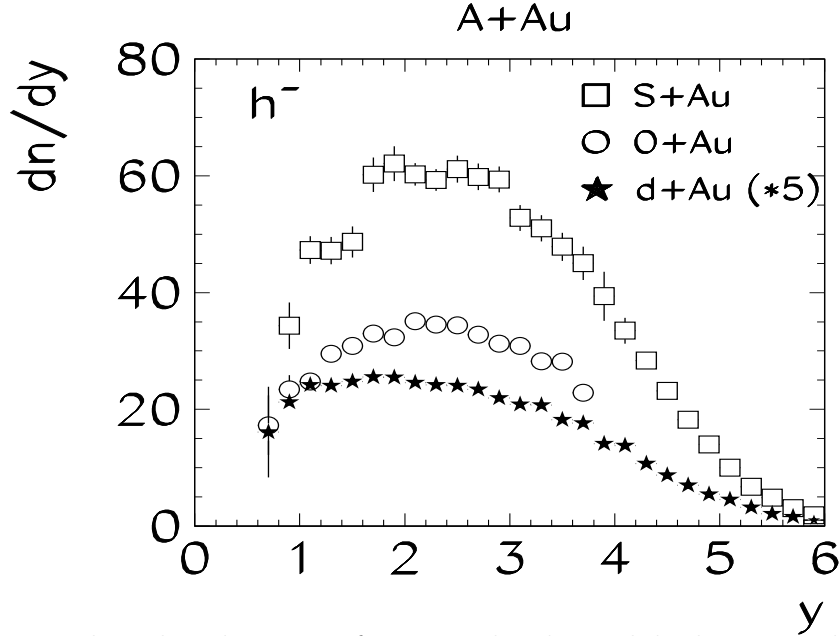

Figure 22. Rapidity distributions of negatively charged hadrons produced in central d+Au, O+Au and S+Au collisions.

6.1.3. Sulphur-Nucleus Collisions

To investigate the target mass dependence for S-induced reactions, rapidity distributions of negatively charged hadrons produced in central S+S, S+Ag and S+Au collisions are compared in Fig. 23. The h^- distribution peaks at midrapidity for the symmetric S+S interactions. The multiplicity increases with the target mass, and the maximum of the distribution moves to lower rapidities with increasing target mass. Fig. 24 shows a comparison of the rapidity distributions of negatively charged hadrons produced in central S+S collisions and in minimum bias nucleon–nucleon interactions. The latter was scaled by the ratio of participant nucleons. The width of the distribution for S+S collisions is slightly narrower than the one for the nucleon–nucleon interactions. The mean negative hadron multiplicity per participant is higher in central S+S collisions than in N+N interactions by about 20%.
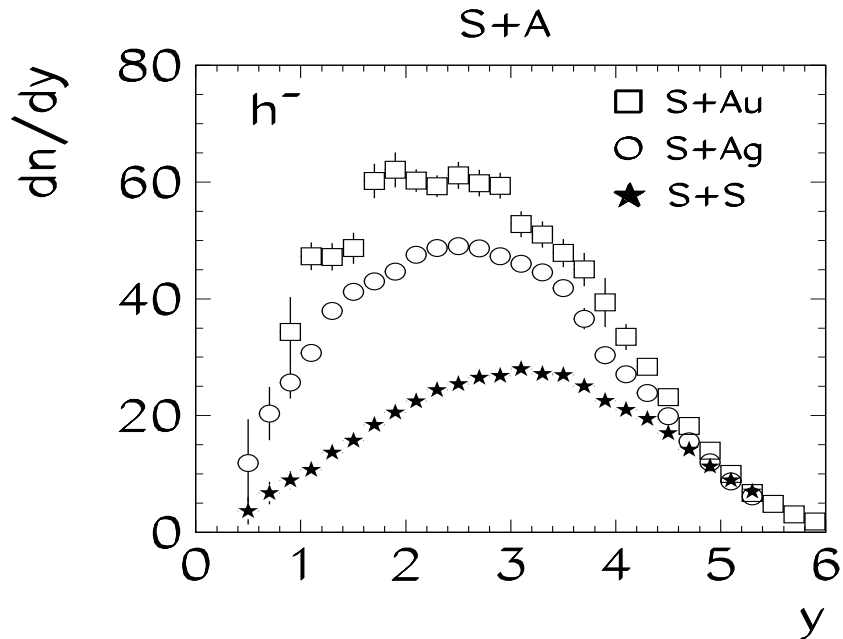
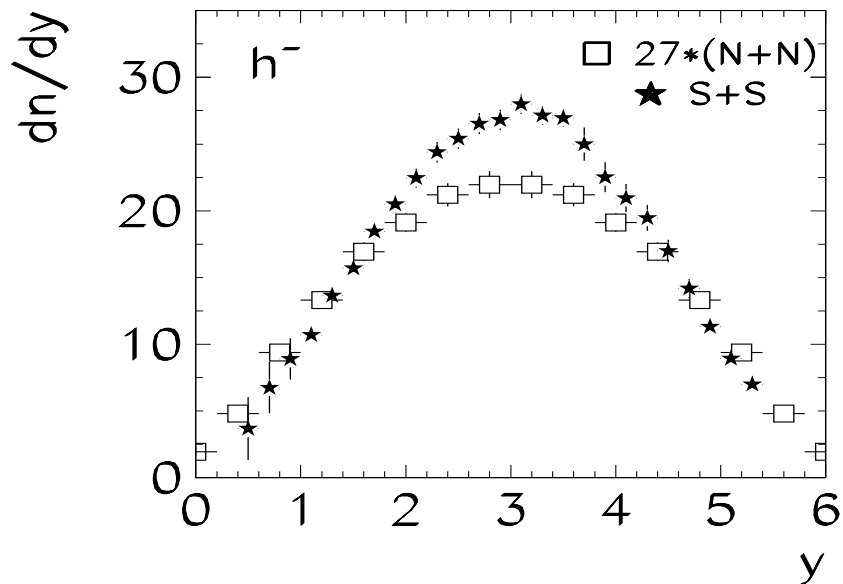Figure 23. Rapidity distributions of negatively charged hadrons produced in central S–nucleus collisions.

Figure 24. Rapidity distributions of negatively charged hadrons produced in central S–S collisions and in minimum bias nucleon–nucleon interactions (scaled by the ratio of participant nucleons).

6.1.4. Extrapolation to 4π

Since the rapidity distributions were measured over a wide kinematic range and cover almost all rapidities between target and beam rapidity, the spectra can be extrapolated to full phase space in order to obtain average total multiplicities. The results are compiled in Table 7. The extrapolation to target and beam rapidity was based on a gaussian fitted locally to the adjacent part of the rapidity distribution. The multiplicities increase with system mass. For comparison average total multiplicities reported from different experiments are also shown. For a review of multiplicities of negatively charged hadrons produced in nuclear collisions cf. [39].

The average multiplicity of negatively charged hadrons increases with the number of net protons. For not too asymmetric systems the ratio of the multiplicity of negatively charged hadrons per net (participant) baryon is shown in Fig. 25. This ratio is smaller in nucleon–nucleon and p+S interactions than in central S+S and S+Ag collisions.

Table 7

Average multiplicity (in acceptance and total) of negatively charged hadrons produced in minimum bias nucleon–nucleon (N+N), minimum bias p–nucleus, deuteron–nucleus and central nucleus–nucleus collisions. The first column lists the reaction, the second column is the measured rapidity range and corresponding average multiplicity and the third column is the extrapolation to 4π acceptance.

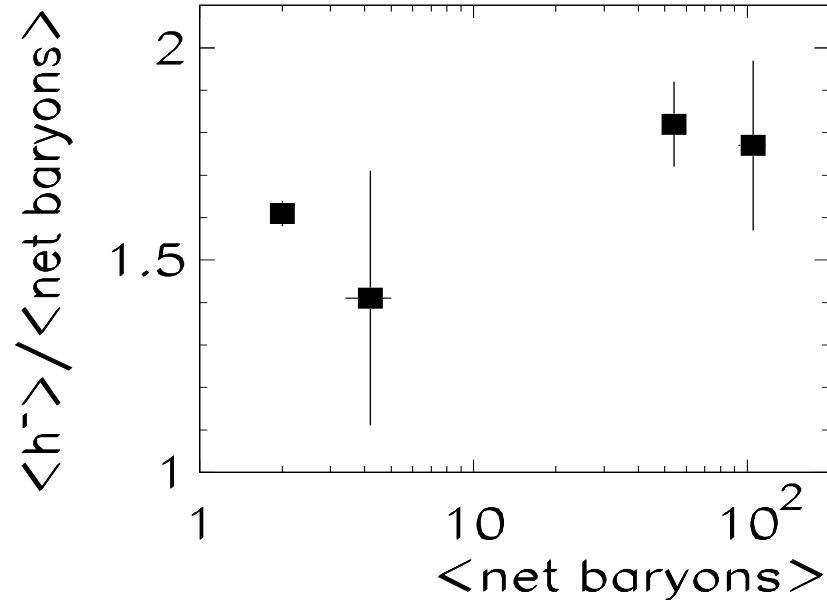| $<h^->$		
Reaction	$0.0 \leq y \leq 6.0$	4π
p+p [35]	-	2.85 ± 0.03
N+N [35]	-	3.22 ± 0.06
p+Mg [37]	-	4.9 ± 0.4
p+S [9]	-	5.0 ± 0.2
p+S	5.7 ± 0.1	5.9 ± 0.2
p+Ar [36]	-	5.39 ± 0.17
p+Ag [37]	-	6.2 ± 0.2
p+Xe [36]	-	6.84 ± 0.13
	$0.8 \leq y \leq 6.0$	4π
p+Au	6.6 ± 0.1	9.9 ± 2
p+Au [37]	-	7.0 ± 0.4
p+Au [38]	-	7.3 ± 0.3
'central' p+Au [8]	-	9.6 ± 0.2
	$0.6 \leq y \leq 6.0$	4π
d+Au	17.2 ± 0.3	23 ± 4
	$0.6 \leq y \leq 3.8$	4π
O+Au	94 ± 2	137 ± 9
O+Au [38]	-	124.0 ± 1.9
	$0.4 \leq y \leq 5.4$	4π
S+S	90 ± 1	98 ± 3
S+S [3]	-	94 ± 5
S+Ag	162 ± 2	186 ± 11
	$0.8 \leq y \leq 6.0$	4π
S+Au	201 ± 2	225 ± 12

Figure 25. Average total multiplicity of negatively charged hadrons per net baryon produced in minimum bias nucleon–nucleon, p+S, central S+S and S+Ag collisions as a function of the number of net baryons.

6.2. Transverse Momentum Spectra

It is important to study the transverse degrees of freedom for produced hadrons in order to learn more about the degree of thermalization in heavy ion collisions and possible effects of collective flow on the spectra. Thermal model fits of the invariant cross sections (see Eqs. 1 and 2) as a function of p_T provide information on the production mechanisms for hadrons. It is known that pions, the majority of the negatively charged hadrons, are to a large part daughters from the decays of heavier resonances. In addition, possible transverse collective flow could further modify the spectra. It is thus not too surprising that the p_T spectra of negatively charged hadrons are, in general, incompatible with thermal parametrizations over the entire p_T-range with the exception of p+S interactions [40, 41, 42, 43, 44]. Since the p_T distributions are found not to be thermal, a systematic analysis using Eq. 2 fits is excluded. Therefore, the h^- data on transverse momentum distributions will be presented systematically without fits in the following sections. However, a fit to Eq. 2 was performed for all systems in the rapidity bin near midrapidity in a limited p_T range ($0.3 \leq p_T \leq 1.0$ GeV/c) in order to give a rough estimate of 'temperatures'.

6.2.1. Proton–Nucleus collisions

The transverse momentum spectra of negatively charged hadrons produced in minimum bias p+S and p+Au collisions are shown in Figs. 26 a,b for four different rapidity intervals: $0.8 < y < 2.0$, $2.0 < y < 3.0$, $3.0 < y < 4.0$, $4.0 < y < 5.0$. The corresponding spectra have been multiplied by the factors of 1000, 100, 10, and 1, respectively, for presentation on the same plot.
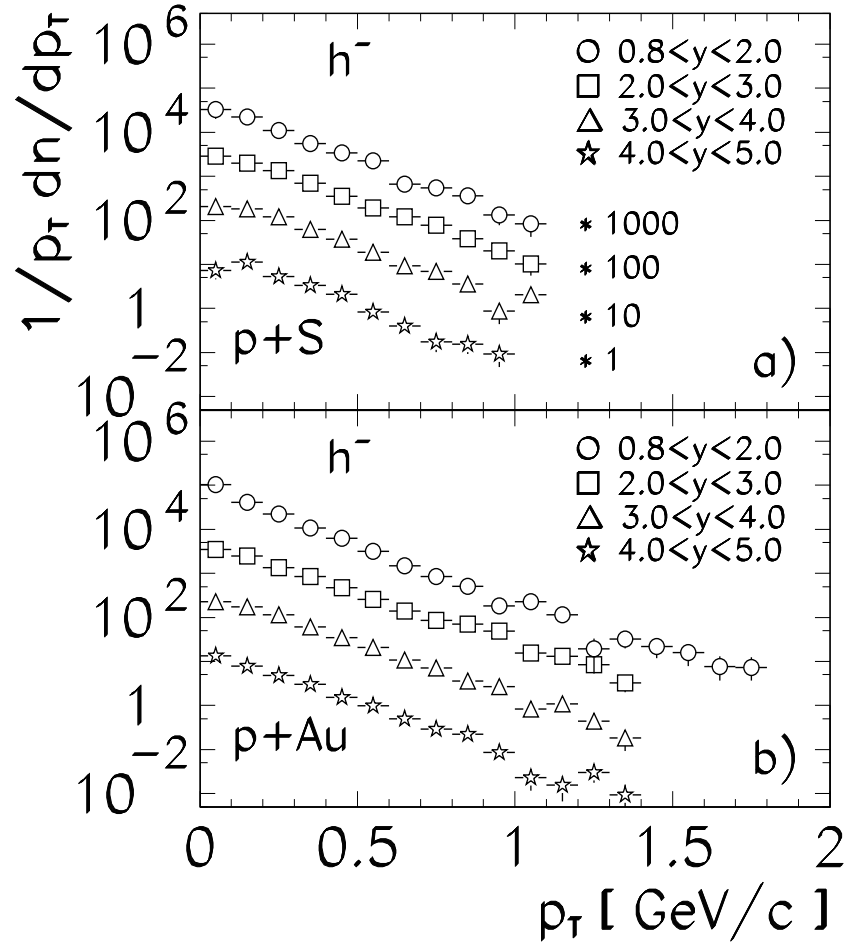
Figure 26. Transverse momentum distributions of negatively charged hadrons produced in p+S (a) and p+Au (b) interactions for the various rapidity intervals shown. The vertical scale is given in $(\text{GeV})^{-2}$.

6.2.2. Nucleus-Nucleus Collisions

The transverse momentum spectra of negatively charged hadrons produced in central d+Au interactions and central O+Au and S+Au collisions are shown in Figs. 27 a-c for various rapidity intervals. The corresponding spectra were multiplied by factors of 1000, 100, 10, and 1, respectively, in the case of d+Au collisions. For the heavy ion collisions the first two spectra (rapidities below midrapidity) were multiplied by factors of 100 and 10. The distributions especially at low rapidities ($0.8 < y < 2.0$) for central O+Au and S+Au collisions clearly exhibit a deviation from a single exponential in p_T with an enhancement at low transverse momenta in the backward rapidity region.
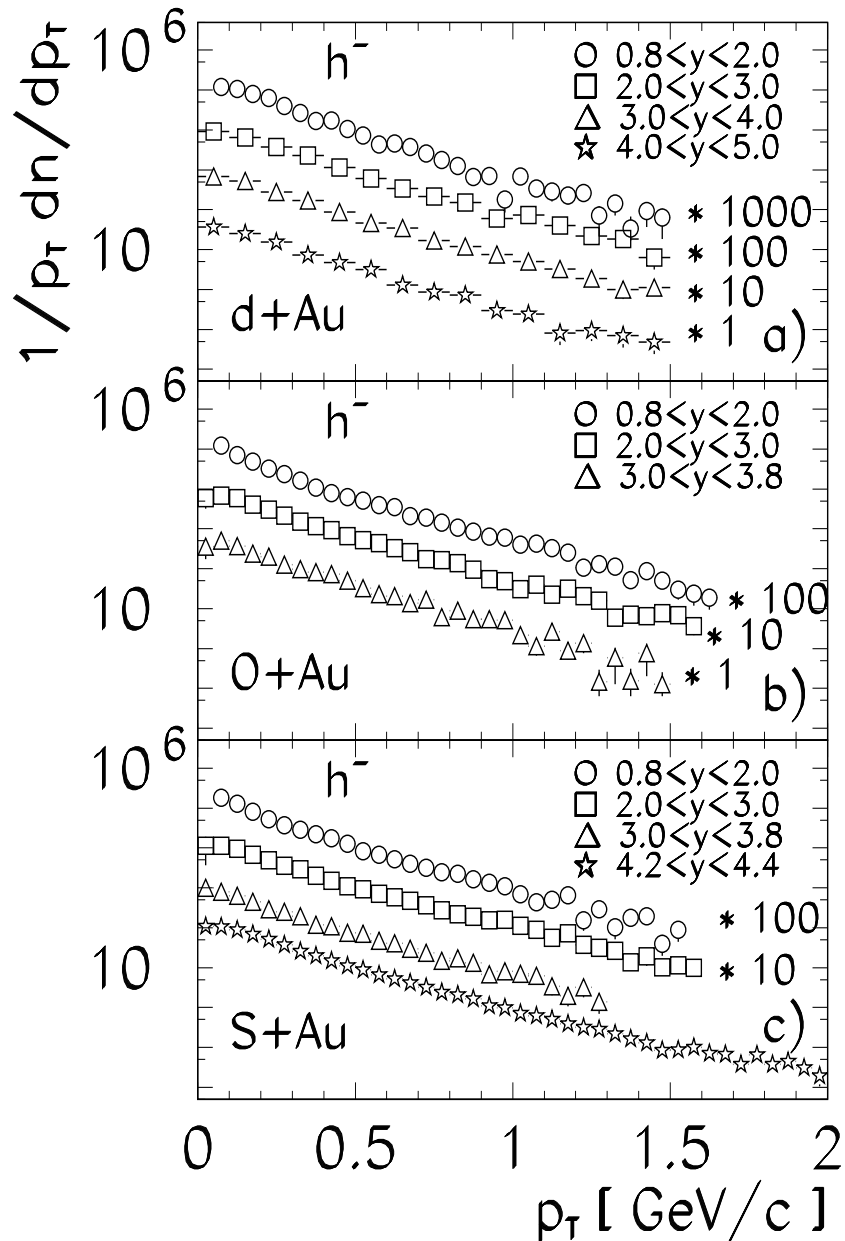

Figure 27. Transverse momentum distribution of negatively charged hadrons produced in central d+Au (a), central O+Au (b) and central S+Au (c) collisions at different rapidities. The vertical scale is given in $(GeV)^{-2}$.

The transverse momentum spectra of negatively charged hadrons produced in central S+S, S+Ag and S+Au collisions are shown in Figs. 28 a-c for various rapidity intervals.
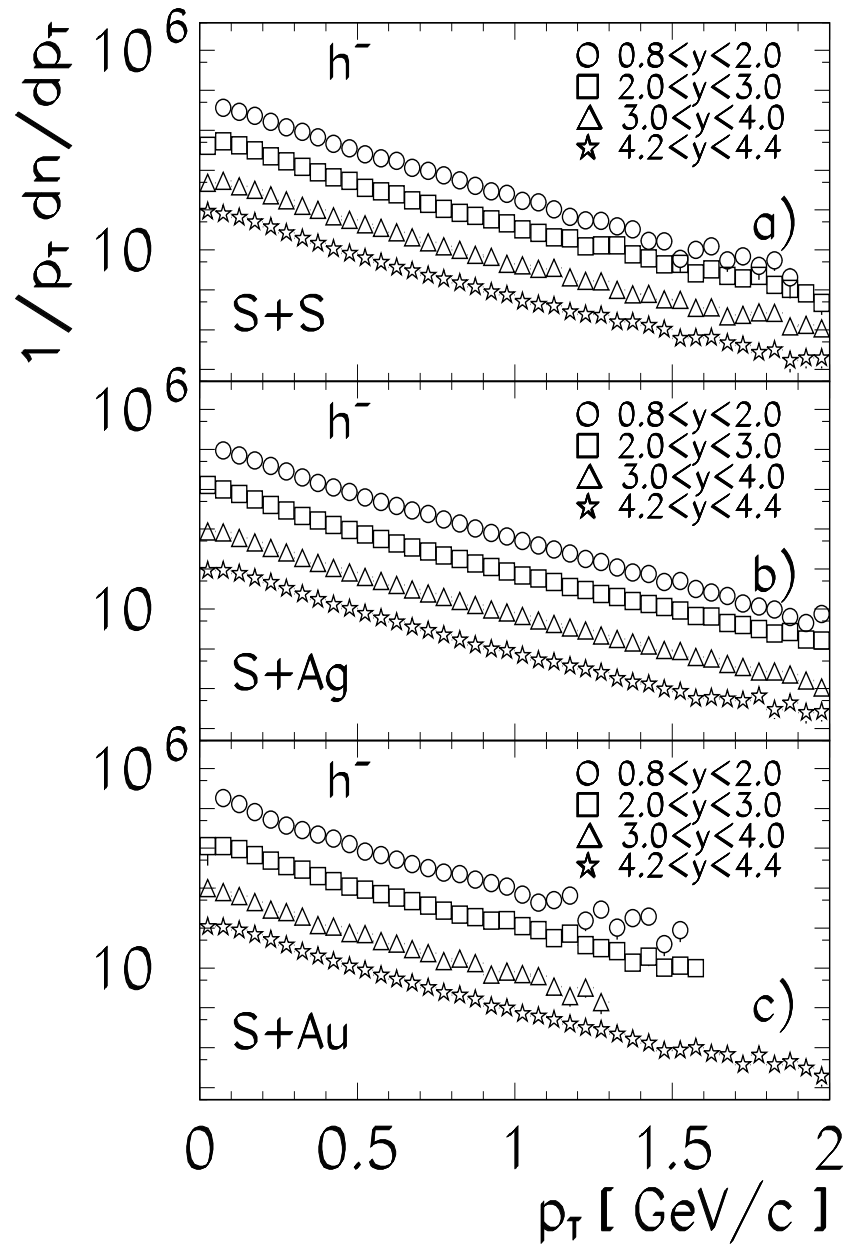

Figure 28. Transverse momentum distribution of negatively charged hadrons produced in central S+S (a), S+Ag (b) and S+Au (c) collisions at different rapidities. The vertical scale is given in $(GeV)^{-2}$.

6.3. Mean transverse momentum

The invariant cross sections of negatively charged hadrons cannot be fitted over the entire p_T range with a single exponential in p_T or m_T. Thus, the mean transverse momentum is calculated for various systems and rapidity intervals, and the results are presented in Table 8. As an example, the rapidity dependence of $\langle p_T \rangle$ in central S+A collisions is shown in Fig. 29. The mean transverse momentum reaches a maximum at midrapidity and exhibits little dependence on rapidity in the vicinity of $y = 3$.

For $y > 4.5$, $\langle p_T \rangle$ decreases rapidly. For the gold target (Fig. 30) there is a slight increase of $\langle p_T \rangle$ in the target hemisphere with the projectile mass. For p+p interactions the $\langle p_T \rangle$ is 340 ± 7 MeV/c for π^- [32, 33, 46] and 366 ± 2 MeV/c for all charged particles in $1.5 < y < 4.5$ [45].
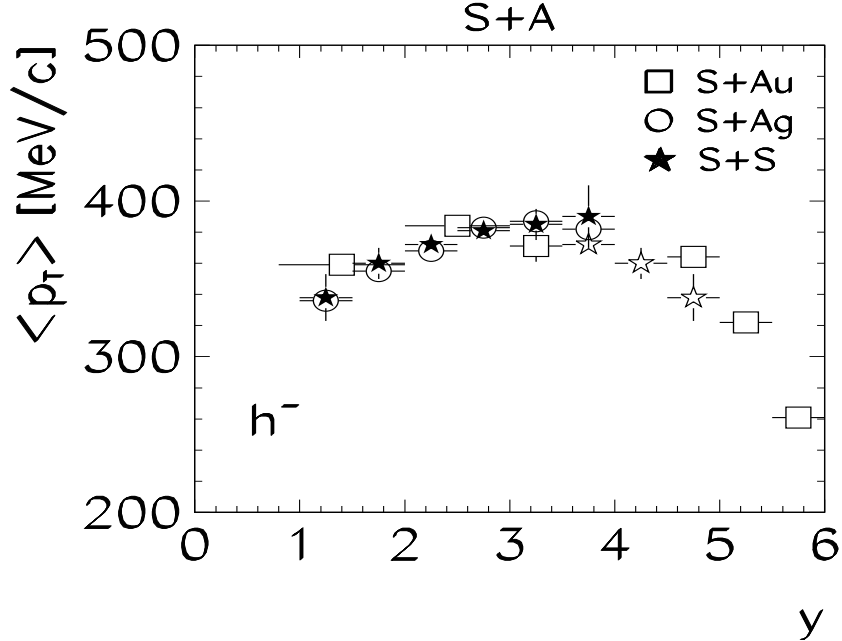

Figure 29. Mean transverse momentum of negatively charged hadrons produced in central S+S, S+Ag and S+Au collisions as a function of rapidity. The open stars are S+S data reflected at $y = 3$.
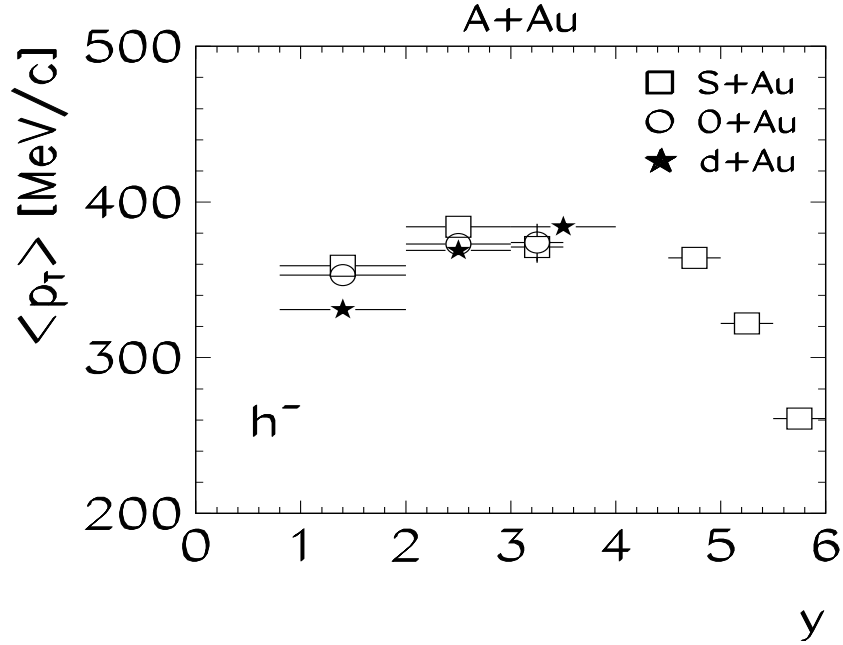
Figure 30. Mean transverse momentum of negatively charged hadrons produced in d+Au, central O+Au and S+Au collisions as a function of rapidity.

Table 8

Mean transverse momenta of negatively charged hadrons produced in p–nucleus, d–nucleus and central nucleus–nucleus collisions for various rapidity intervals. The systematic error is less than 10 MeV/c.

$< p_T > [MeV/c]$			
Reaction	$0.8 \leq y \leq 2.0$	$2.0 \leq y \leq 3.0$	$3.0 \leq y \leq 4.0$
p+S	325 ± 6	363 ± 8	335 ± 8
p+Au	311 ± 5	377 ± 6	372 ± 7
d+Au	331 ± 4	369 ± 5	384 ± 5
	$0.8 \leq y \leq 2.0$	$2.0 \leq y \leq 3.0$	$3.0 \leq y \leq 3.5$
O+Au	353 ± 5	373 ± 4	374 ± 12
S+S	349 ± 9	377 ± 4	388 ± 11
S+Ag	346 ± 2	376 ± 1	385 ± 1
S+Au	359 ± 6	384 ± 5	371 ± 10
	$4.5 \leq y \leq 5.0$	$5.0 \leq y \leq 5.5$	$5.5 \leq y \leq 6.0$
S+Au	364 ± 2	322 ± 3	261 ± 4

6.4. Inverse slope parameters

To facilitate comparison with other published results (see Table 10) fits to Eq. 2 were performed in the interval $0.3 \leq p_T \leq 1.0$ GeV/c. The resulting inverse slope parameters T are listed in Table 9. A typical result of such a fit is shown in Fig. 31 which indicates an overall discrepancy between the concavely shaped data and the rather straight to convex curve corresponding to Eq. 2. The fit is thus carried out in the restricted range only, and this has always to be kept in mind in comparing to other results concerning h^- and π^-. Below 250 MeV/c the data points are all above the fit. This enhancement (*low p_T enhancement*) is most pronounced at low rapidities in collisions with heavy targets [47]. Fitting p+p data in a similar way and averaging the results from different experiments yields an inverse slope parameter at midrapidity of 142 ± 10 MeV [31, 34, 40, 41, 48].

Table 9

Inverse slope parameters T_2 (Eq. 2, fitted to the data in the interval $0.3 \leq p_T \leq 1.0$ GeV/c) of negatively charged hadrons produced in p-nucleus, d-nucleus and central nucleus-nucleus collisions for various rapidity intervals.

	T_2 [MeV]			
Reaction	$0.8 \leq y \leq 2.0$	$2.0 \leq y \leq 3.0$	$3.0 \leq y \leq 4.0$	$4.0 \leq y \leq 5.0$
p+S	159 ± 13	169 ± 13	154 ± 10	142 ± 12
p+Au	150 ± 8	183 ± 10	177 ± 9	171 ± 10
d+Au	151 ± 9	165 ± 10	181 ± 12	183 ± 11
	$0.8 \leq y \leq 2.0$	$2.0 \leq y \leq 3.0$	$3.0 \leq y \leq 3.8$	$4.2 \leq y \leq 4.4$
O+Au	189 ± 5	188 ± 8	175 ± 10	-
S+S	175 ± 4	191 ± 7	191 ± 6	186 ± 5
S+Ag	184 ± 2	199 ± 2	201 ± 4	185 ± 5
S+Au	182 ± 7	200 ± 10	190 ± 10	187 ± 5

Table 10

Inverse slope parameters T_2 (Eq. 2, fitted to the data in the interval $0.3 \leq p_T \leq 1.0$ GeV/c) of negatively charged hadrons in comparison with other experiments.

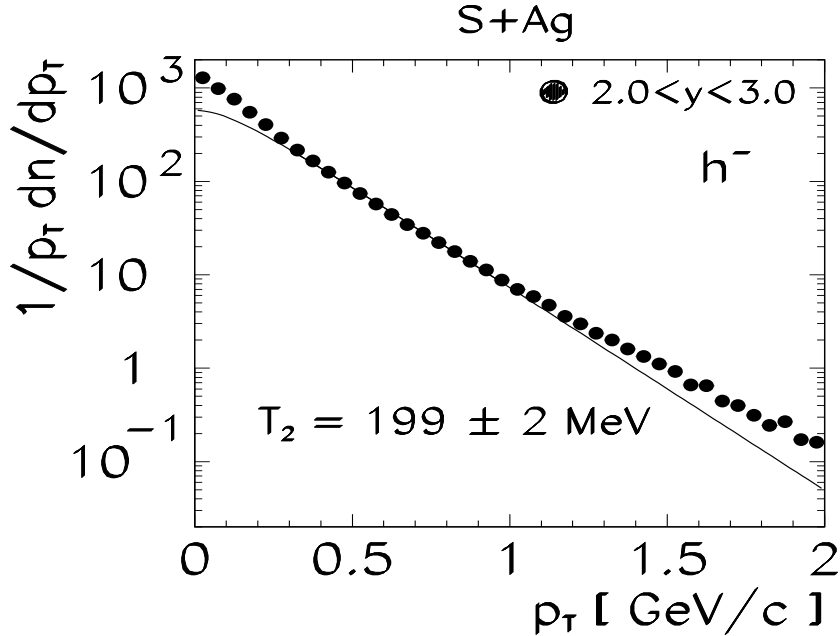| T_2 [MeV]		
	this paper h^-	NA34 [43] h^-
Reaction	$0.8 \leq y \leq 2.0$	$1.0 \leq y \leq 1.9$
p+Au/W	150 ± 8	161 ± 5
O+Au/W	189 ± 5	167 ± 5
S+Au/W	182 ± 7	165 ± 5
	this paper h^-	NA44 [27, 31] π^- $0.25 < m_T - m_0 < 1$ GeV/c^2
Reaction	$3.0 \leq y \leq 3.8$	$3.0 \leq y \leq 4.1$
S+S	191 ± 6	148 ± 4
S+Au/Pb	190 ± 10	156 ± 8

Figure 31. Transverse momentum distribution of negatively charged hadrons produced in central S+Ag collisions. The solid line is a fit of Eq. 2 to the data in the interval $0.3 < p_T < 1.0$ GeV/c. The vertical scale is given in (GeV)$^{-2}$.

The average transverse momentum of negatively charged hadrons exhibits only a slight increase with the system size, measured by the average total multiplicity of the collision, as shown in Fig. 32, whereas the temperature of the net protons increases from about 150 MeV in p–nucleus to 200 MeV in central O+Au collisions and about 240 MeV in central S–nucleus collisions (Fig. 33).
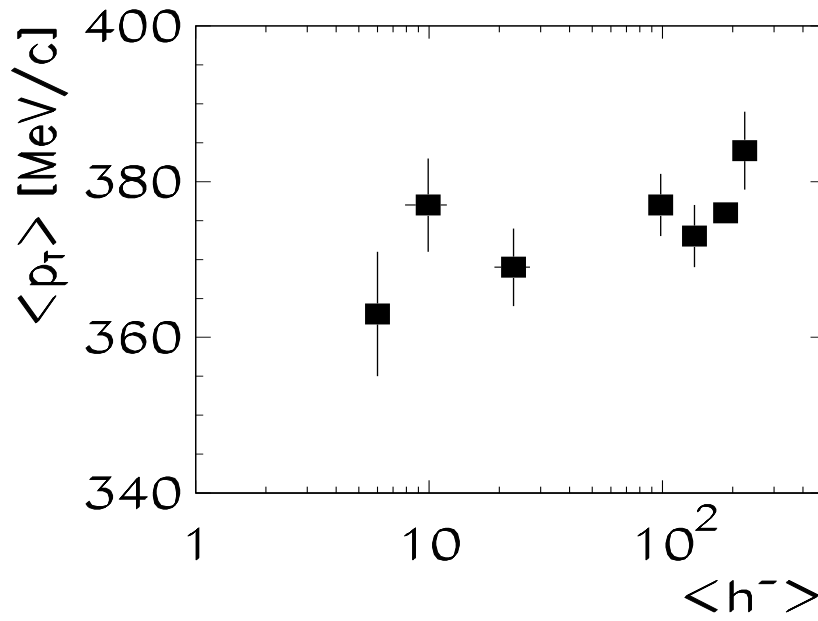

Figure 32. Average transverse momentum in $2 < y < 3$ of negatively charged hadrons produced in p–nucleus, deuteron–nucleus and nucleus–nucleus collisions as a function of the average multiplicity.
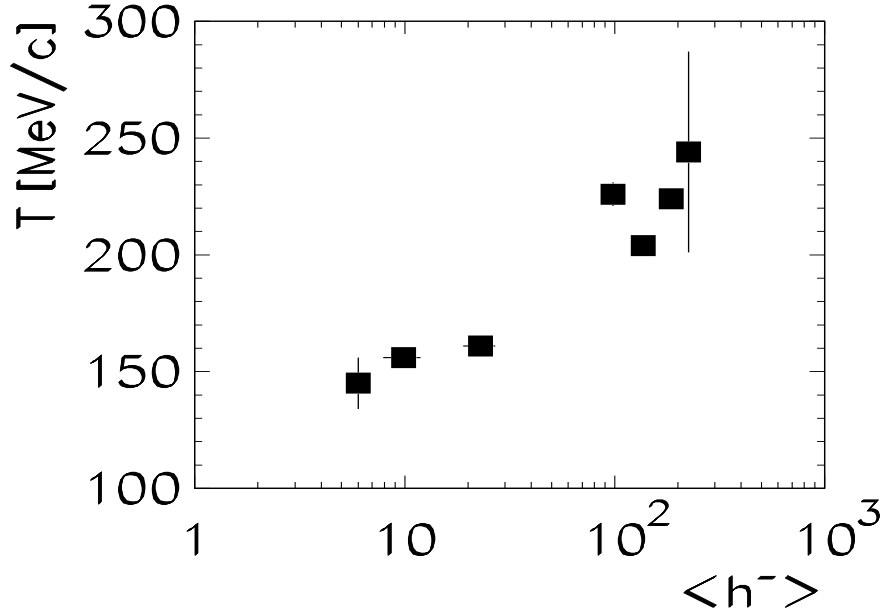
Figure 33. 'Temperature' of net protons for p–nucleus, deuteron–nucleus and central nucleus–nucleus collisions as a function of the average multiplicity of negatively charged hadrons.

7. Summary

We have presented results of a systematic study, using the NA35 experiment at CERN, of rapidity and transverse momentum distributions of net protons and negatively charged hadrons. A large part of this data was analyzed employing a new automatic analysis technique developed by NA35. The most significant findings are:

1) The shape of the rapidity distributions of net projectile protons $(p - \overline{p})$ is similar for d+Au, central O+Au and central S+Au collisions. From this we conclude that the stopping of projectile nucleons is independent of the size of the (light) projectile nucleus when incident on a heavy target nucleus (Au in this study). This suggests that there is no significant difference in the stopping mechanism as inferred from the proton rapidity for these light incident nuclei.

2) The average rapidity loss $\langle \delta y \rangle$ for projectile protons which participate in the interaction is $\langle \delta y \rangle = 1.2$ - 1.6 for various projectiles from protons to sulphur incident on a sulphur target and $\langle \delta y \rangle = 2.0$ - 2.3 for a gold target. The $\langle \delta y \rangle$ are found to be approximately independent of the projectile mass for projectile masses ranging from protons to sulphur. Thus, the rapidity loss of projectile participant protons increases with the nuclear thickness of the target and is approximately independent of the nuclear thickness of the lighter projectile as might be expected.

3) The number of net protons at midrapidity increases with projectile mass and with target mass. Since the mean rapidity shift measured for interacting projectile protons increases with target mass up to $\langle \delta y \rangle = 2.0$ - 2.3 for a gold target and since the rapidity

region for 200 GeV/nucleon incident energy is a total of $y_{proj} - y_{targ} = 6$, it is expected that the total number of protons at midrapidity ($y = 3$) will increase with both projectile and target mass. This results in a significant pile-up of protons at midrapidity for the heavier systems.

4) The transverse momentum distributions for net protons ($p - \overline{p}$) can be described by thermal distributions with 'temperatures' ranging from T $\approx$ 140 MeV for p + S near target rapidity to T $\approx$ 245 MeV for central S + S and S + Au collisions at midrapidity, using Eq. 1. Such inverse slope parameters are much higher than the Hagedorn temperature ($T \approx$ 150 MeV) and cannot be considered to be true thermal freeze-out temperatures. Our results may indicate the presence of radially ordered transverse flow in central S+A collisions.

5) The average negative hadron multiplicity increases with both the target and projectile masses. The mean negative hadron multiplicity per participant is higher in central S+A collisions than in N+N interactions by about 20%.

6) The mean transverse momentum of negatively charged hadrons at midrapidity is approximately independent of the mass of the incident nuclei. There is a decrease in the mean transverse momentum when going away from midrapidity. This is observed for all colliding systems of this study.

7) The spectra of negatively charged hadrons do not have a simple thermal shape. They exhibit deviations (above a thermal spectrum) at low ($p_T <$ 250 MeV/c) and high ($p_T >$ 1 GeV/c) transverse momenta. These significant deviations may be due to transverse collective flow and resonance production and decay as well as to the 'Cronin effect'.

REFERENCES

1. *Proc. 11th Int. Conf. on Ultra-Relativistic Nucleus-Nucleus Collisions (Quark Matter 1995)*, Monterey, California, USA (1995), ed. by A.M. Poskanzer, J.W. Harris and L.S. Schroeder, *Nucl. Phys.* **A590** (1995).

2. *Proc. 12th Int. Conf. on Ultra-Relativistic Nucleus-Nucleus Collisions (Quark Matter 1996)*, Heidelberg, Germany (1996), ed. by P. Braun-Munzinger, H.J. Specht and R. Stock, *Nucl. Phys.* **A610** (1997).

3. J. Bächler et al., NA35 Collaboration, *Phys. Rev. Lett.* **72** (1994) 1419.

4. H. Sorge, *Z. Phys.* **C67** (1995) 479, **C71** (1996) 178 (erratum).

5. U. Ornik et al., *Phys. Rev.* **C54** (1996) 1381; J. Bolz, U. Ornik and R.M. Weiner, *Phys. Rev.* **C46** (1992) 2047.

6. J. Sollfrank et al., *Z. Phys.* **C61** (1994) 659; E. Schnedermann, J. Sollfrank and U. Heinz, *Phys. Rev.* **C48** (1993) 2462.

7. J. Bächler et al., NA35 Collaboration, *Z. Phys.* **C52** (1991) 239.

8. A. Bamberger et al., NA35 Collaboration, *Z. Phys.* **C43** (1989) 25.

9. J. Bartke et al., NA35 Collaboration, *Z. Phys.* **C48** (1990) 191.

10. J. Bächler et al., NA35 Collaboration, *Z. Phys.* **C58** (1993) 367.

11. T. Alber et al., *Z. Phys.* **C64** (1994) 195.

12. K. Werner, *Phys. Rev. Lett.* **62** (1989) 2460.

13. J. Cleymans and H. Satz, *Z. Phys.* **C57** (1993) 135.

14. P. Braun-Munzinger et al., *Phys. Lett.* **B365** (1996) 1.

15. A. Leonidov, M. Nardi and H. Satz, *Z. Phys.* **C74** (1997) 535.

16. D. Brinkmann et al., *Nucl. Inst. and Meth.* **A354** (1995) 419.

17. S. Wenig, *GSI-90-23 Report* (1990).

18. J.W. Harris et al., *Nucl. Inst. and Meth.* **A315** (1992) 33.

19. T. Alber et al., NA35 Collaboration, *Phys. Lett.* **B366** (1996) 56.

20. G. Roland, Univ. of Frankfurt PhD thesis (1992).

21. B. Andersson, G. Gustafson and B. Nilsson-Almqvist, *Nucl. Phys.* **B281** (1987) 289.

22. R. Brun et al., *GEANT3 User Guide* CERN/DD/EE/84-1 (1986).

23. H. Appelshäuser, Diploma thesis, Univ. of Frankfurt, GSI-93-09 Report (1993).

24. L.P. Teitelbaum, PhD thesis, LBL-32812, Berkeley (1992).

25. S.R. Tonse et al., NA35 Collaboration, *Nucl. Phys.* **A525** (1991) 689c.

26. D. Röhrich, "Hadron Production in Nucleus-Nucleus Collisions at SPS- and AGS-Energies", pp. 505-516 in *Hot and Dense Nuclear Matter*, ed. by W. Greiner, H. Stöcker and A. Gallmann, (NATO ASI Series B: Physics Vol. 335), New York and London: Plenum Press, 1994.

27. J. Dodd, NA44 Collaboration, *Nucl. Phys.* **A590** (1995) 523c.

28. F. Videbaek and O. Hansen, *Phys. Rev.* **C52** (1995) 2684.

29. A. Wróblewski, Acta Phys. Polonica **B16** (1985) 379.

30. A. Białas, M. Błeszyński, W. Czyż, *Nucl. Phys.* **B111** (1976) 461.

31. I.G. Bearden et al., NA44 Collaboration, *Phys. Rev. Lett.* **78** (1997) 2080.

32. A.M. Rossi et al., *Nucl. Phys.* **B84** (1975) 269.

33. T. Kafka et al., *Phys. Rev.* **D16** (1977) 1261.

34. M. Adamus et al., *Z. Phys.* **C39** (1988) 311.

35. M. Gaździcki and O. Hansen, *Nucl. Phys.* **A528** (1991) 754.

36. C. De Marzo et al., *Phys. Rev.* **D26** (1982) 1019.

37. D.H. Brick et al., *Phys. Rev.* **D39** (1989) 2484.

38. J. Bächler et al., NA35 Collaboration, *Z. Phys.* **C51** (1991) 157.

39. M. Gaździcki and D. Röhrich, *Z. Phys.* **C65** (1995) 215.

40. B. Alper et al., *Nucl. Phys.* **B100** (1975) 237.

41. K. Guettler et al., *Nucl. Phys.* **B116** (1976) 77.

42. J.W. Cronin et al., *Phys. Rev.* **D11** (1975) 3105.

43. T. Åkesson et al., HELIOS Collaboration, *Z. Phys.* **C46** (1990) 361.

44. H. Bøggild et al., NA44 Collaboration, *Z. Phys.* **C69** (1996) 621.

45. C. De Marzo et al., *Phys. Rev.* **D29** (1984) 363.

46. J. Whitmore, *Phys. Rep.* **C10** (1974) 273.

47. D. Röhrich et al., NA35 Collaboration, *Nucl. Phys.* **A566** (1994) 35c.

48. Y. Cho, *Phys. Rev. Lett.* **31** (1973) 413.